University of Nevada, Reno

Automated Design and Optimization of Metallic Alloys

A thesis submitted in partial fulfillment of the

requirements for the degree of Master of Science in Materials Science & Engineering

By

Jake Hohl

Leslie T. Mushongera/Dissertation Advisor

December 2021

University of Nevada, Reno

THE GRADUATE SCHOOL

We recommend that the thesis
prepared under our supervision
by

Jake Hohl

entitled

**Automated Design and
Optimization of Metallic Alloys**

be accepted in partial fulfillment of
the requirements for the degree of

MASTER OF SCIENCE

Leslie T. Mushongera, Ph.D.
Advisor

Yufeng Zheng, Ph.D
Committee Member

Pradeep Menezes, Ph.D.
Graduate School Representative

David W. Zeh, Ph.D., Dean
Graduate School

December, 2021

1. Abstract

The design and optimization of metallic alloys poses a significant engineering challenge. The search space of all possible alloys is sufficiently large that it is impossible to fully explore by traditional methods. In order to address this challenge, physics based computational frameworks linked to advanced machine learning algorithms can serve to automate this process with computational efficiency such that the state of the industry may be rapidly advanced. The work herein presents a suite of computational frameworks leveraged to automate the design and optimization process of advanced alloys. An ab initio alloy thermodynamics system, Molecular Dynamics simulations, a Convolutional-Neural Network system, and a coupled Neural Network and Multi-objective Genetic Algorithm. These algorithms are validated over the set of binary nanocrystalline Al-X alloys, and multi-component High Entropy Alloys (HEA).

2. Acknowledgements

Firstly, I would like to thank my advisor, Dr. Leslie T. Mushongera, for his support and guidance over the last year. His council and patience have been invaluable and has shaped my experience at UNR. I would especially like to thank him for his understanding and regard for personal wellbeing. Thank you to my UNR Computational Materials peers for their contributions and willingness to share their knowledge and expertise. Their advice and collaboration will always be appreciated. Most of all, thank you to my family and girlfriend Irene for their support; without them I would not be here.

3. Table of Contents

4. List of Tables

5. List of Figures

Figure 1. Summary of Molecular Dynamics simulations of nanocrystalline Al-Mg deformation mechanisms. (I) grain boundary interface cracking (II) grain boundary dissociation (III) twin deformation (IV) grain boundary interface curvature effects (V) interface dislocation nucleation site (VI) grain boundary void formation (VII) dislocation.

Figure 2. Grain boundary dissociation mechanism, dislocations along the grain boundary with orthogonal Burgers vectors (purple).

Figure 3. Grain boundary atomic motion effect on interface cracking (I) crack forming in the wake of atomic flow (II) crack forming at interface impingement.

Figure 4. Void formation, dislocations close off a portion of the crystallite interior which forms an internal void.

Figure 5. Dislocation layering and localized slip.

Figure 6. Atomic flow, direction of applied load. Atomic displacement is denoted by yellow vectors.

Figure 7. Mechanical response under tension (a) pure nanocrystalline Al (b) nanocrystalline Al-Mg(10%).

Figure 8. Components of the microstructure by volume (a) pure nanocrystalline Al (b) nanocrystalline Al-Mg(10%).

Publication 3:

Figure 1. Computational framework structure, sub-sectioned into three tasks: microstructure creation, image pre-processing, and feature recognition.

Holistically these components map input image data to classification labels as output.

Figure 2. Flattening Layer, utilized by the CNN used to format the feature map for use by the final classification step of the algorithm, the output layer.

Figure 3. Dense Layer, used to facilitate the final classification step of the algorithm, and provide full connectivity of the network layers.

Figure 4. Detail of the CNN's structure. Operations used to map the input data to output data are shown as well as their connectivity.

Figure 5. Model interface implemented in Tkinter, used to label image data for training of the algorithm.

Figure 6. Input data format, numerically encoded image data represented as a 256 palleted color scale pixel array.

Figure 7. Simulated microstructure image data produced by Voronoi Tessellation coupled to Molecular Dynamics.

Figure 8. Resultant classified images denoting correctly and incorrectly classified features.

Figure 9. Sci-kit Learn classification report, denoting the classification performance of the algorithm over each feature set.

Figure 10. Algorithm classification accuracy evolution by epoch. Matching trend between training accuracy and validation accuracy denotes lack of overfitting.

Publication 4:

Figure 1. Feedforward Backpropagation Neural Network.

Figure 2. Non-dominated Sorting Genetic Algorithm.

6. Introduction

The research in this thesis details an effort to democratize and improve the advanced metallic alloy design process through utilizing machine learning and physics-based simulation. Alloy thermodynamics, Molecular Dynamics, deep Neural Networks, Convolutional Networks, and multi-objective Genetic Algorithms are developed and applied to the design of nanocrystalline binary alloys and multi-component high-entropy alloys.

Utilized as the first validating dataset, nanocrystalline metal alloys are those in which the average microstructural crystallite size is in the nanometer range, typically defined to be less than 100 nm. This grain refinement from a traditional alloy is typically achieved through mechanical alloying or advanced processing methods, such as spark-plasma sintering, that aim to control the solidification rate of the metal as an indirect method of controlling crystallite size. A small average crystallite size corresponds to a large volume-fraction of grain boundaries in the material's microstructure as the thickness of the grain boundaries is not significantly reduced as the crystallite size decreases. Being that disordered grain boundaries in polycrystalline metals serve as impediments for dislocation motion, dislocation mobility is reduced in nanocrystalline metals relative to conventional microcrystalline metals. This reduction in mobility is accompanied by an increase in strength and reduction in ductility. Certain material processing techniques, such as post-processing heat treatment, are able to regain some ductility in the material. As such, nanocrystalline materials can provide superior mechanical properties to conventional alloys. However, an increased volume fraction of disordered grain boundaries serves to

increase the free energy of the microstructure. Because the system is driven towards an energy minimizing state, this increased free energy is driven towards reduction through crystallite enlargement by the annihilation of grain boundaries and the coalescence of crystallites. Therefore, this process reduces the improved material properties initially gained through crystallite size reduction. In order to avoid this loss of properties, dopant elements are added to the base nanocrystalline metal that tend to segregate to the grain boundaries of the material. These dopant elements are chosen such that they have a preferentially tendency for segregation over forming a solid solution in the crystallite region. Via this segregation, at the grain boundaries of the material, the free energy of the disordered system is reduced via grain boundary relaxation, effectively reducing or eliminating the driving force for grain growth. However, chosen dopant elements must also be stable against the precipitation of secondary phases in the base nanocrystalline element as this precipitation serves to consume a portion of the active dopant element thereby reducing its efficacy in causing free energy reduction at the grain boundaries. This research details a thermodynamic framework applied to the set of binary nanocrystalline Al-X systems for which microstructural stability is predicted against grain enlargement and the precipitation of secondary phases.

In the case of nanocrystalline metals, significant research in the area of crystal plasticity and the deviations between microcrystalline and nanocrystalline deformation mechanisms is currently underway. During an average crystallite size reduction from the microcrystalline to nanocrystalline range it has been shown that a transition from slip-based deformation to grain boundary mediated processes occurs. This change in the dominant deformation regime heavily influences the dominant deformation mechanisms in the

materials' microstructures, specifically grain boundary migration and slip. This research details Molecular Dynamics studies of nanocrystalline Al-Mg(10%) in its segregated state, for which thermodynamic stability against both grain enlargement and phase precipitation is predicted under uniaxial tension in order to identify these mechanisms in stabilized materials and hypothesize their correlation to material properties.

Effective analysis of material test and simulation data also poses a significant challenge to advanced alloy design. Typically, microstructural image data is analyzed through the use of a researcher's expertise and direct comparisons to previous studies; an example of which can be seen in the analysis of NC Al-Mg in this work. Initially, automation of this process was done through the use of expert systems. These systems were designed as databases of labeled microstructural image data specific to a material class and configuration; pairwise comparisons of this data to slices of the input data forms the classification process. While relatively accurate, this process is very computationally expensive, data-intensive, and lacks adaptability. In order to address these challenges, early machine learning based classification algorithms, such as Support Vector Machines, were used. These algorithms significantly reduced the computational cost of the classification process, as well as providing a small reduction in the completeness in volume of the supporting datasets needed. However, these algorithms came at the cost of accuracy. This research details an object-based Convolutional Neural Network system, the current state of the industry in image classification algorithms. This solution retains high accuracy while reducing computational cost and is fully adaptable across datasets and even material classes.

As the second validating dataset, High Entropy Alloys are typically comprised of up to twelve alloying elements and are defined as those which possess significant components of five or more elements. Complex interactions between these components are responsible for their improved strength densities and resistance to fractures while specific properties of a given material are primarily driven by crystalline structure. Typically, HEA's inherently have a trade-off in properties, as do most classes of alloys. Thermal stability, hardness, yield strength, ductility, and fatigue life vary across alloy classes and between BCC and FCC structures. For this reason, effective design of this class of alloys is a significant challenge. Additionally, processing techniques of these alloys are limited to relatively small-scale methods such as spark-plasma sintering and liquid phase synthesis. Furthermore, those techniques which have been proven successfully at manufacturing bulk quantities of HEA's are limited in the purity of the produced samples. As such, sample synthesis poses and additional significant challenge to effectively designing and testing high entropy alloys. This research details a computational framework comprised of a coupled Regression Neural Network and Non-dominated Sorting Genetic Algorithm to effectively propose high entropy alloy designs and assess their efficacy on the basis of cost and predicted material properties.

By combining the current state of research in the field of advanced alloys with the current best performing predictive and generative machine learning algorithms, the work herein develops a basis and toolset to aid materials researchers during the materials design process. The design loop formed utilizes Molecular Dynamics simulations in order to develop a dataset of simulated materials consisting of their compositions related to their mechanical response, a coupled Neural Network and Genetic Algorithm learns the pattern

in these property-composition relationships and generates and optimizes material designs based on these predictions. The thermodynamics framework can then be used to screen these proposed and optimized designs for thermodynamic stability resulting in a final design alloy set. These optimal and stable alloys can be further assessed in terms of their detailed deformation mechanisms and mechanical response by additional physics-based Molecular Dynamics studies. By this process, alloys can be designed, assessed, and investigated in detail rapidly and adaptably.

7. Publications

This thesis consists of the following four papers, written to address these challenges in advanced alloy design and formatted for publishing in scientific journals.

Paper 1: Pages 13-37 have been published in the Journal of Materials Science

Paper 2: Pages 38-49 will be submitted for publication in Materials Letters in a condensed form

Paper 3: Pages 50-66 have been submitted for publication in the Journal of Computational Materials

Paper 4: Pages 67-81 have been submitted for publication in the Journal of Computational Materials

I. Paper 1

Thermodynamic Stabilization of Nanocrystalline Aluminum

Jacob Hohl[1,*], Pankaj Kumar[1,2], Mano Misra[1], Pradeep Menezes[3,] Leslie T Mushongera[1,*]

[1]Department of Chemical & Materials Engineering, University of Nevada, Reno, Reno, NV, 87557, USA
[2]Department of Mechanical Engineering, University of New Mexico, Albuquerque, NM, 87106, USA
[3]Department of Mechanical Engineering, University of Nevada, Reno, Reno, NV, 87557, USA
**Corresponding authors: lmushongera@unr.edu, jhohl@unr.edu*

Abstract – Nanocrystalline metals are generally unstable due to a large volume fraction of high-energy grain boundaries associated with a small grain size. Preferential dopant segregation to the high-energy grain boundaries is observed to enhance the stability of the material's microstructure by minimizing its energy. Nanocrystalline aluminum-dopant systems were evaluated for thermodynamic stability against grain growth and phase precipitation via the mechanism of grain boundary segregation according to a modified regular nanocrystalline solution model. Fifty-one potential dopant elements have been evaluated for their efficacy in stabilizing nanostructures with three potential candidates, magnesium, lanthanum, and silicon, identified possessing the characteristics to promote grain boundary segregation and a state of thermodynamic stability in aluminum's nanocrystalline regime. The minimum dopant content required to achieve nanocrystalline microstructure stability is identified for each of the three candidate elements. Beyond this

minimum content, further addition of the dopant elements decreased the final microstructure's stability with no effects on the existence of a stable nanocrystalline state.

1. Introduction

Nanocrystalline metals are comprised of ultra-fine grains with diameters of typically less than 100 nm [1,2]. Due to the small size of the constituent grains, large fractions of atoms are positioned at or near grain boundaries, compared to conventional polycrystalline metals with coarse grains [2,3]. As a result of this structure, nanocrystalline metals exhibit superior mechanical properties as compared to their polycrystalline counterparts. The extraordinary mechanical properties of nanocrystalline metals include high ductility at room temperature, high hardness and high strength [3–5]. The hardness of nanocrystalline metals has been observed to be up to seven times higher than in coarse-grained materials [4]. Additionally, the yield strength of nanocrystalline metals can be up to ten times higher than of coarse-grained materials [6–9]. These unique qualities are attributed to the large fraction of interfacial materials present within the grain boundaries. It is thus apparent that the nanoscale grain size in nanocrystalline metals brings about a significant increase in the strength of the materials.

Despite the impressive mechanical properties, nanocrystalline metals are restricted to use in real application, largely due to the microstructural instability. Retaining the morphology and size of the constituent grains in nanocrystalline metals is a major challenge to successfully use in the many applications over a long period of time. The compromised stability of nanocrystalline metals originates from the excess energy due to the high-volume fraction of grain boundaries in these ultra-fine grained structures [10–13]. This

complexity is associated with both the highly degenerate nature of grain boundary structures as well as the interconnected nature of the boundary network within nanocrystalline microstructure. In the grain boundary region, atoms are typically shifted from their regular lattice sites to accommodate the mismatch between the adjacent grains causing high-energy configurations [1]. As a result, grain boundaries are associated with an excess stored energy compared to the grain interior. This excess stored energy provides a driving force for grain coarsening – a detrimental microstructural phenomenon which is characterized by the growth of the large grains at the expense of smaller ones. A coarse-grained structure is thermodynamically favored since it has less excess stored energy due to a smaller grain boundary volume as compared to a nanocrystalline structure. Due to this excess stored energy, nanocrystalline metals coarsen rapidly even at low temperatures and lose their extraordinary mechanical properties [7]. This highlights that the grain size, as widely accepted, is not the only structural feature of interest for nanocrystalline materials. The grain boundary state considerably alters the thermodynamic and mechanical stability of the materials. Therefore, it must be the focus when designing nanocrystalline materials.

To retain the properties of nanocrystalline materials in bulk components for structural applications, stabilization of the nanostructure with respect to coarsening is highly desirable. An ideal metallic nanostructure is one in which the as-manufactured grain morphologies and sizes are preserved, regardless of exposure conditions [7]. It is imperative that the characteristic nanocrystalline grain size, and high-volume fraction of grain boundaries be retained in the long-term in order to preserve the material's extraordinary properties. To enhance the stability of the nanocrystalline metals, the excess stored energy in the grain boundaries should be reduced [1]. The preferential decoration of

grain boundaries with dopants provides a potentially promising approach to stabilize the NC structure [10, 11]. Recent theories have suggested that through the addition of dopant elements in small amounts to pure nanocrystalline metals, the interfacial free energy associated with a high-volume fraction of grain boundaries in the material can be reduced. In some cases, the interfacial energy can be reduced below the free energy of the bulk solution, thereby eliminating the driving force required for grain growth, which results in a stable segregated nanocrystalline state [8-10]. The precise mechanism by which this happens is still a subject of conjecture. Several mechanisms have been proposed to explain how nanocrystalline metals are strengthened by grain boundary segregation. In one of these mechanisms, the partitioning of dopants to the grain boundaries in nanocrystalline metals increases the atomic registry at the boundaries, which shifts the energy of the grain boundary atoms to lower value [14]. Along with a reduction in the grain boundary energy [11-13], a contribution to the impediment of grain boundary motion from Zener drag exists [14-15]. Via this mechanism, dopants at the grain boundaries have also been suggested to mechanically restrict the migration of grain boundaries significantly, thus reducing coarsening.

Precipitation of secondary intermetallic phases due to the presence of dopants is one of the processing challenges which can disrupt the necessary segregation required for grain stability and strength. When the concentration of the added dopant is in a supersaturated state in the nanocrystalline matrix, such thermodynamic conditions will promote second phase precipitates to nucleate and grow in the grain interiors. In general, the second phase precipitates in metallic materials are often considered to serve as obstacles to dislocation glide and cause hardening of the material [15]. This notion, however, fails to explain recent

discoveries of high-strength and large-ductility materials with a high density of these precipitates, as obstacles to dislocation glide leading to high stress concentration and even microcracks. Most often these deleterious secondary intermetallic phases are brittle in nature which negatively affects the mechanical properties of the material. Furthermore, the formation of the coarse, incoherent precipitates along grain boundaries leads to softening and substantially reduces the fracture resistance of these materials [16–18]. To achieve the best possible effect from grain boundary stabilization through the addition of segregation of dopants, it is necessary to identify the stable nanocrystalline thermodynamic states that do not form precipitates.

To realize this, an understanding of the principles of thermodynamics, and how these principles can be harnessed to achieve stable nanocrystalline structure, is required. In order to model the thermodynamics of both grain boundary segregation and the formation of solid solutions, the thermodynamics of the solid state can be employed. The primary concept from which thermodynamic stabilization mechanisms of nanocrystalline solids is built is that nature trends towards minimizing the energy state of a natural system. This concept is tied to the concept of entropy or disorder, is generated during any thermodynamic process. An ideal system may generate no disorder, i.e., its entropy generation is zero, but entropy may never be annihilated by a thermodynamic process [19]. To this end, if a thermodynamic formulation that describes the variation in the energy state of a system can be established, it can be said that the point at which this energy is minimized will be the stable state of the system, towards which it will trend. Additionally, the energy itself is neither created nor destroyed, it is only conserved and converted between forms. This provides the concept of enthalpy, or the energy which is necessary for

a process to occur [19]. These process enthalpies are the driving forces for thermodynamically driven change; in the specific case of this research, these enthalpies will be the driving forces for the segregation of atoms and for the formation of solid solutions.

Traditionally, thermodynamic modeling of nanocrystalline materials has evolved from the basis of describing solute segregation energetically [20]. Weissmuller was one of the first to quantitatively describe that a reduction in grain boundary energy can be achieved through the segregation of solute atoms to a nanocrystalline material's grain boundaries [21]. This concept was formulated from the Gibbs Adsorption Isotherm, and the works of Birringer [22], who was the first to propose the theory. From Weissmuller's description of solute partitioning utilizing the Langmuir-McLean segregation equation, Liu and Kirchheim were able to formulate a relationship between the bulk and grain boundary solute contents that specifically described solute segregation for binary nanocrystalline alloys [23]. From this relationship, Kirchheim described the conditions that would lead to metastability of nanocrystalline materials [23]. Weissmuller expanded upon Kirchheim's criteria to create a regular solution model for a binary polycrystalline alloy system in terms of bond energies and number of bonds in each of the grain boundary, intercrystalline, and transition regions of the material [21]. It is important to note that Kirchheim's work neglected the elastic and mechanical effects of solute segregation. This shortcoming was in part rectified by Trelewicz and Schuh [24], and then fully described by Saber and Chookajorn [25,26]. The resulting models were applied to binary systems with a positive enthalpy of mixing by Murdoch and Schuh [27], to ternary alloy systems by Saber [28],

and in a modified state to binary systems with both positive and negative enthalpies of mixing in this work.

The objective of this work is to establish the conditions to stabilize the grain structure of nanocrystalline aluminum (NC Al). Based on thermodynamic principles, a highly efficient dopant design framework has been used to identify the specific dopants that interact with high energy grain boundaries in NC Al to release the excess free energy in the boundaries. It is of interest to improve the stability of the NC Al not only against grain growth, but also against phase separation. The dopant design framework is based on a modified regular solution model to describe the free energy state of the nanocrystalline structure in terms of bond energies and thermodynamic parameters.

In Section 2, the thermodynamic framework and analytical methods used in this work are presented. Section 3 describes the results and discussion before concluding in Section 4.

2. Thermodynamic Framework

To assess the efficacy of various dopants in stabilizing NC Al, a standard regular solution model for binary nanocrystalline alloys is adopted [27]. The nanocrystalline structure is modeled as two physically and chemically distinct regions in nanocrystalline metals namely: the ordered crystalline bulk (c) and the disordered grain boundary (gb). The energetics of the system is described by a mixing free energy which is formulated with separate energetic interactions for the two regions in the nanostructure. The crystalline bulk and the grain boundary are however not treated as separate phases, per se, but are considered to be geometrically connected to one another such that the global dopant content of the nanocrystalline structure satisfies the mass balance

$$X = V_{gb}X_{gb} + \left(1 - V_{gb}\right)X_c \qquad (1)$$

where, X_{gb} is the concentration of a dopant species in the grain boundary region, X_c is the concentration of a dopant species in the crystalline bulk. Treating the two regions as geometrically connected will allow such that a reduction in grain size, *d*, will cause an increase in the grain boundary volume fraction, V_{gb}, which follows a cubic scaling

$$V_{gb} = 1 - \left(\frac{d - \xi}{d}\right)^3 \qquad (2)$$

where, ξ is the width of the transition region which is smeared over a finite distance and is composed of bonds between atoms in the crystalline bulk and in the grain boundary. The width of the transition region will be taken as 0.5 nm [27] in all the following. The geometry of the nanocrystalline metal is postulated as a distribution of atomic bonds between the crystalline bulk, grain boundary and transition region. The energies associated with such a geometry is contained in the final free energy function of explicit form

$$\Delta G^{mix} = \left(1 - V_{gb}\right)\Delta G_c^{mix} + V_{gb}\Delta G_{gb}^{mix} + zvV_{gb}\left(X_{gb} - X_c\right)\left[\left(2X_{gb} - 1\right)\omega_{gb} - \frac{1}{zt}\left(\Omega^B\gamma^B - \Omega^A\gamma^A\right)\right] \qquad (3)$$

This expression is a solution model for a binary system, in which grain size is a state variable and grain boundary segregation contribute strongly to the energetics of the system. The subscripts denote the crystalline bulk (*c*) and grain boundary (*gb*), and the superscripts denote the two chemical species, A (Al solvent) and B (dopant). γ^A and γ^B are the interfacial energies of pure Al and the dopant, respectively. The other terms are associated

with the geometrical way in which those two regions interact. The parameters z, Ω and v are the coordination number of the bulk material, the atomic volume and the fraction of atoms contributing bonds to the transitional bonding region, respectively. The interaction parameters are related to the enthalpy terms that describe the tendency of the solute atoms to mix into the solvent as a solid solution or segregate to the grain boundary respectively, with positive values of the corresponding parameter indicating a higher preference for each tendency. The interaction parameter in the grain boundaries (ω_{gb}) is related to the enthalpy of segregation (ΔH_{seg}) as

$$\omega_{gb} = 2\omega_c - \frac{2\Delta H_{seg}}{z} - 2\frac{\Omega^B\gamma^B - \Omega^A\gamma^A}{2zt} \qquad (4)$$

This captures the thermodynamics of the grain boundary environment, which incorporates chemical interactions, elastic mismatch, and the mismatch in interfacial energies. The interaction parameter in the bulk grain (ω_c) is related to the enthalpy of mixing (ΔH_{mix}) following

$$\omega_c = \frac{\Delta H_{mix}}{zX(1-X)} \qquad (5)$$

The free energy function in Eq. (3) is essentially in the form a modified regular solution model in the limit of infinite grain size and will also reproduce a grain boundary energy in the proper limit. The estimate values of the enthalpy of mixing for fifty-one aluminum-dopant binary systems are obtained using [29],

$$\Delta H_{mix} = \left[X_A X_B\left(X_B^s \Delta H_{AinB}^{int} + X_A^s \Delta H_{BinA}^{int}\right)\right]_{ch} + \left[X_A X_B (X_B \Delta H_{AinB}^{elastic} + X_A \Delta H_{BinA}^{elastic})\right]_{elastic} + \Delta H_{ss}^{structura} \qquad (6)$$

where X_A and X_B are the compositions of the dopant and the Al solvent, respectively, and X_A^S and X_B^S are effective fractions of the surface of dopant atoms in contact with Al atoms and vice versa. This describes the difference in interaction between a B atom surrounded by A atoms, and one surrounded by some mixture of A and B atoms, dictated by composition. $\Delta H_{ss}^{structural}$ is the enthalpy of the formation of a solid solution of the dopant element in the matrix of the solvent. $\Delta H_{AinB}^{elastic}$ accounts for the elastic strain effects caused by solute atoms expanding or contracting the lattice of the solvent, if they are larger or smaller than the solvent atoms respectively. Chemical interactions are captured by the terms of form ΔH_{BinA}^{int} which describe, e.g., the enthalpy of a B atom completely surrounded by A atoms. Furthermore, grain boundary segregation enthalpies are calculated as [30],

$$\Delta H_{seg} = -0.237v\left[-\Delta H_{BinA}^{int} - c_0\gamma_A^S V_A^{\frac{2}{3}} + c_0\gamma_B^S V_B^{\frac{2}{3}}\right] + \Delta E_{el} \qquad (7)$$

the term $c_0\gamma_A^S V_A^{\frac{2}{3}}$ is the surface enthalpy of a pure metal where $c_0 = 4.5 \times 10^8$ is a dimensionless semi empirical constant, V is the atomic volume, and γ_A^S is the surface energy of the pure subscripted component. The coefficient captures the change in coordination at the surface; when the segregant B atom is at the surface rather than in the bulk, it has gone from being surrounded by A atoms to being only two-thirds in contact. The coefficient 0.237 accounts for the surface relaxation due to surface electron density distribution and surface geometry, which reduces the exposed surface area. ΔE_{el} accounts for the elastic strain effects that contribute to segregation [31].

$$\Delta E_{el} = \frac{24\pi K_A G_B r_B r_A (r_A - r_B)^2}{3K_A r_A + 4G_B r_B} \qquad (8)$$

where, *K* is the bulk modulus, *G* is the shear modulus, r is the atomic radius.

The terms ΔG_c^{mix} and ΔG_{gb}^{mix} can be postulated to describe the extremes in the thermodynamic state of a nanocrystalline system in which either only the bulk crystal or grain boundary exists. In a sharp grain boundary limit, i.e., the thickness of the grain boundary region is infinitesimally small, $d \to 0$, only a single crystal exists, which reduces Eq. (3) to a classical regular solution

$$\Delta G_c^{mix} = z\omega_c X_c(1 - X_c) + kT[X_c lnX_c + (1 - X_c)\ln(1 - X_c)] \qquad (9)$$

where k is the Boltzmann constant and T is the temperature. On the other extreme end when $d = t$, a hypothetical system with only the grain boundary exists which again simplifies Eq. (3) to

$$\Delta G_{gb}^{mix} = z\omega_{gb} X_{gb}\left(1 - X_{gb}\right) + \frac{\Omega^A \gamma^A}{t}\left(1 - X_{gb}\right) + \frac{\Omega^B \gamma^B}{t} X_{gb} + kT[X_{gb} lnX_{gb} + \left(1 - X_{gb}\right)\ln\left(1 - X_{gb}\right)] \qquad (10)$$

Considering the co-existence of both the bulk crystal and grain boundary, the global thermodynamic state can then be postulated as an interpolation of Eqs. (9) and (10) in addition to the interaction parameters accounting for the transition region which yields Eq (3). This equation yields a 3D free energy surface in grain boundary composition–grain size space as shown in Fig. 1. This free energy surface describes how the material system's energy changes as a function of its grain boundary solute content (X_{gb}), which is an approximation for the system's degree of segregation, and as a function of the final

microstructure's average grain size (d). Therefore, this surface shows the most prominent and influential variable quantities that affect the degree of stability that the nanocrystalline structure is capable of attaining. A nanocrystalline minimum in this surface denotes a state of stability at which the benefit to material properties of a nanocrystalline microstructure are retained. By using Eq. (1) in (3), the nanocrystalline stability can be evaluated as a function of the global dopant content.

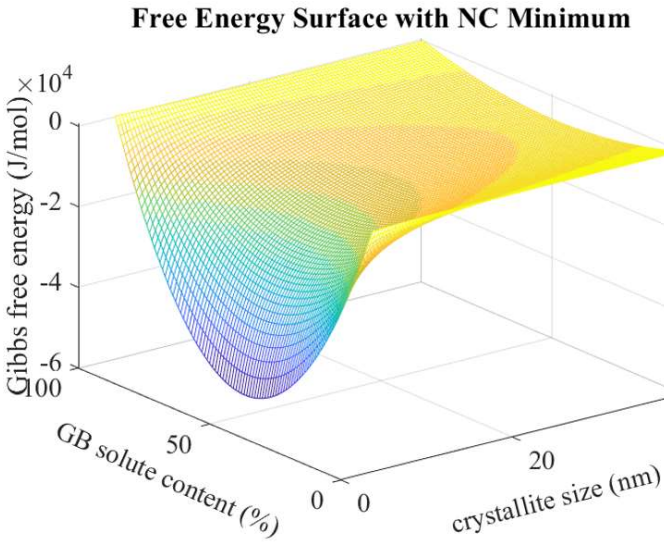

Figure 1. Schematic of a Gibbs free energy surface with a minimum in the grain boundary region. The energy minimizing grain boundary dopant content and the preferred grain size correspond the minimum in the free energy surface.

An important feature of this approach is that it will not only identify the dopant compositions that lead to a reduction in the grain boundary energy but will also identify the stable grain size. These quantities for the stable state of the material system can be directly read from the corresponding axes of the generated free energy surface at which a minimum occurs, as seen in Figure 1. This effect can be clearly seen in the 2D plot in Figure 2, where the blue line is the free energy curve for the nanocrystalline state of the material, and the red line is the free energy of the

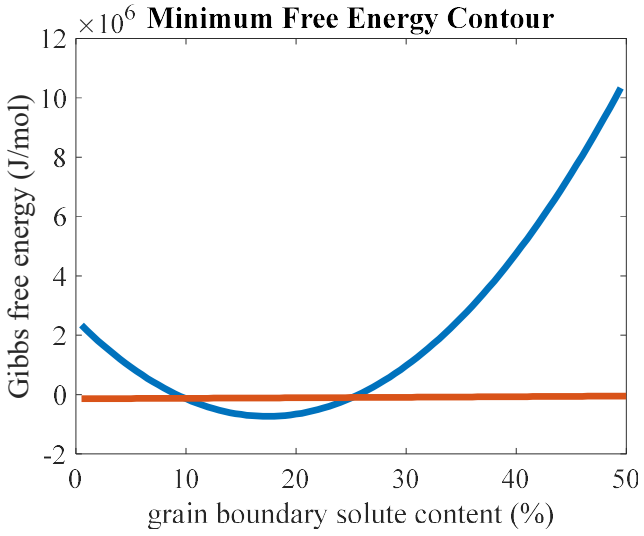

Figure 2. Gibbs free energy plot showing the energy minimizing grain boundary solute content corresponding to the minimum in the energy surface. Blue line denotes nanocrystalline state, red line denotes bulk large-grained state.

bulk unsegregated large-grained material. If the nanocrystalline state's curve is concave in shape, as determined by sign of its second derivative, and any point on the curve exhibited a free energy value lower than that of the material system's unsegregated bulk solution, a stable nanocrystalline state exists. Otherwise, the most energetically favorable state for the material system is that of the bulk solution at a large grain size, attainable by the occurrence of grain growth.

3. Results and Discussion

3.1 Analysis of grain boundary segregation

Through use of the regular nanocrystalline solution model (Eq. (3)), NC Al has been evaluated for thermodynamic stability through grain boundary segregation using fifty-one potential dopants. The input parameters used in the model were obtained from literature. The two thermodynamic parameters, which together contain all of the most relevant physics of the problem: enthalpies of segregation and mixing were obtained for all of the fifty-one systems from Ref. [29]. All other material parameters, including pure substance grain boundary energies and atomic volumes, were obtained from [24,26,27,32,33]. To form stability surfaces based on Eq. (3) throughout the entire design space for each binary Al-dopant system, the grain size was varied from 10 to 100 nm and grain boundary solute content was varied throughout its whole range of 0 to 100 at%. This variation was performed in steps of 1%, in order to provide sufficient resolution to accurately determine the stable state of the system.

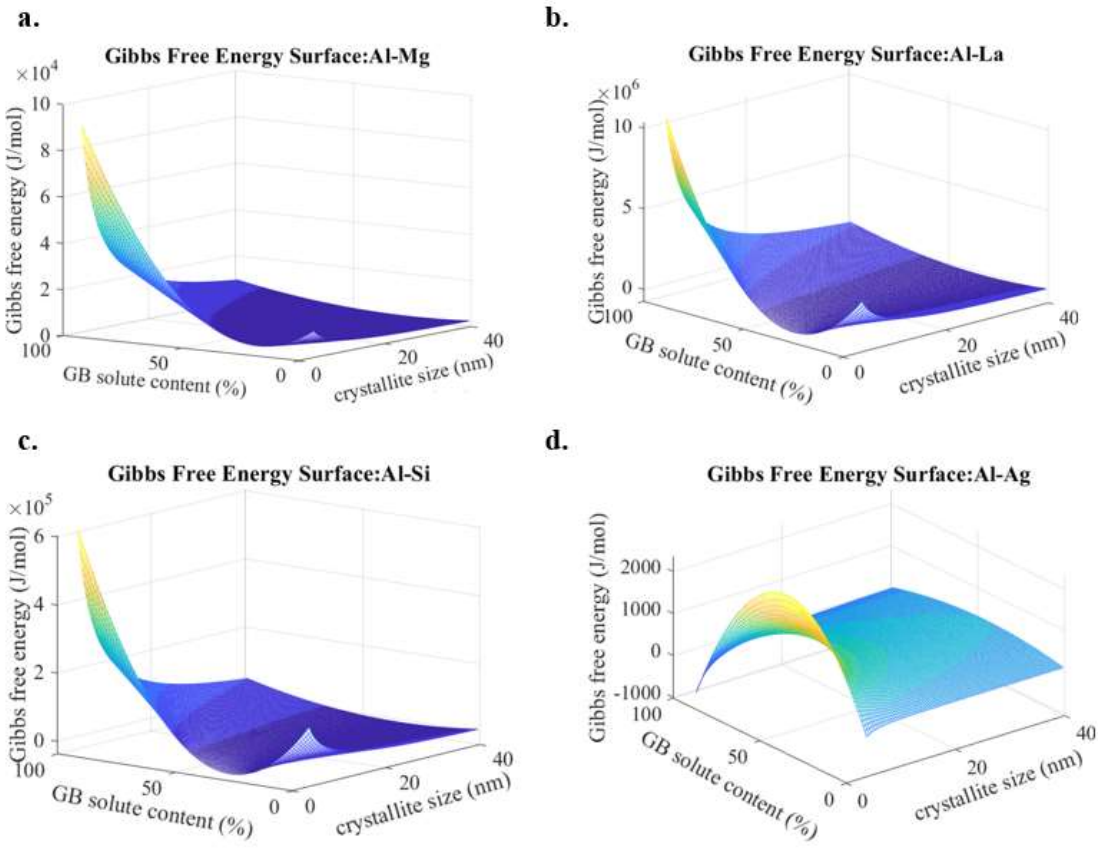

Figure 3. Gibbs free energy surfaces as function of the grain boundary dopant content, X_{gb} and grain size, d for (a) NC Al-Mg (b) Al-La (c) Al-Si and (d) Al-Ag systems, for a global dopant content of $X = 10\%$.

Using the fifty-one dopant elements, free energy surfaces were constructed and utilized to create a set of stability predictions for binary NC Al-dopant systems. This stability was achieved through free energy minimization at the grain boundary regions. 3D Gibbs free energy surfaces were constructed for each NC Al-dopant combination to assess thermodynamically stable nanocrystalline states and global compositions. From these studies three candidate dopants: magnesium (Mg), lanthanum (La), and silicon (Si), were selected as exhibiting the necessary characteristics to segregate to the grain boundary and provide a stable nanocrystalline state. This selection was done by examining the free energy surfaces created for each material and identifying surfaces exhibiting minima in the

grain boundary dopant content-grain size regime. A unique characteristic of each of the three identified dopants is that they possess positive enthalpy of segregation; due to this fact, these three exhibits a tendency for segregation towards the grain boundaries. However, of the three, only Mg possesses a positive enthalpy of mixing [29]. Being that this thermodynamic characteristic describes the solute's ability to form a solid solution with the Al solvent, Mg may be identified as the most promising dopant for binary Al systems. From a thermodynamics perspective, a positive enthalpy of mixing implies that the solvent and dopant atoms do not have an affinity for each other thus essentially separate out leading to the dopants segregating to the disordered grain boundaries. Additionally, since the regular nanocrystalline regular solution empirical stability criterion (see Section 3.4) is only valid for positive enthalpy of mixing systems, Mg is the only dopant for which the model confidently predicts stability against phase precipitation. Figure 3 shows the necessary minima in the Gibbs free energy surfaces for NC Al-Mg, Al-La, Al-Si, and Al-Ag systems, respectively, where (a)-(c) show stable nanocrystalline states whereas (d) shows an unstable nanocrystalline state. This distinction can be seen by the concavity of the surface, as determined by its second derivative. Concave surfaces result in stable nanocrystalline minima, while convex surfaces denote instability of the microstructure with respect to grain growth. As such, in Al-Mg, Al-La, Al-Si nanocrystalline systems, the grain boundary segregated state is energetically favorable to that of the large-grained bulk solution. On the other hand, Al-Ag in Fig. 3(d) with a convex free energy surface will always have an unstable nanocrystalline structure thus will be susceptible to grain coarsening. By evaluating the grain boundary solute content (X_{gb}) and grain size (d) at which the minima in the free energy occur, the degree of segregation and the resultant

microstructure's grain size can be predicted. For a global dopant content of $X = 10\%$, a maximum achievable grain boundary dopant content $X_{gb,Mg} = 25\%$ was predicted for Al-Mg, $X_{gb,La} = 35\%$ for Al-La, and $X_{gb,Si} = 34\%$ for Al-Si. The dopant content at which the nanocrystalline minimum occurs is a function of the degree of segregation that a material system exhibits. Therefore, it is dependent on the enthalpy of segregation, and is different for each solvent-solute pair. In the case of binary aluminum systems, a global Mg content of 13% was found to promote the highest degree of stability for the Al-Mg nanocrystalline system. 10% La or Si content was necessary for stability, with higher contents corresponding to smaller final crystallize sizes without affecting the existence of a stable state

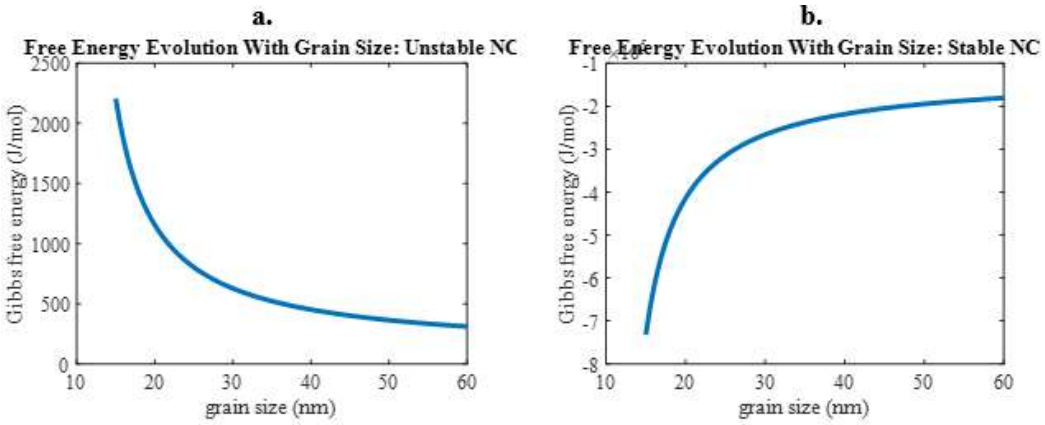

Figure 4. Evolution of Gibbs free energy with grain size for (a) unstable and (b) stable nanocrystalline state.

Additionally, the three stable nanocrystalline systems show a minimum achievable grain size of 10 nm. However, the actual grain size that can be achieved during manufacturing is ultimately dependent on the initial grain size of the raw aluminum powder that is alloyed to create the segregated system as well as the processing methods and conditions. Smaller initial grain sizes typically result in smaller grain sizes in stabilized

nanocrystalline systems. Figure 4 shows the variation in Gibbs free energy, as a function of grain size, for both the case of an unstable nanocrystalline state and a stable nanocrystalline state. It can be seen that, for an unstable nanocrystalline material, the free energy of the system decreases with an increase in grain size. Being that the energy minimized state is thermodynamically stable, this shows that the stable microstructure in this case is that of a bulk large-grained material. In contrast to this, for the case of a stable nanocrystalline state, it can be seen that the energy minimum occurs at a small nanoscale microstructure, with the free energy of the large-grained microstructure being greater than that of our stable nanocrystalline state. The resulting plots of Gibbs free energy vs grain size can in essence be used as a quick tool for identifying material systems for which a stable nanocrystalline state exists.

3.2. Stability against second phase precipitation

It is likely that the dopant element interacting with the solvent element could lead to the formation of second phase precipitates once the maximum solubility limit within the

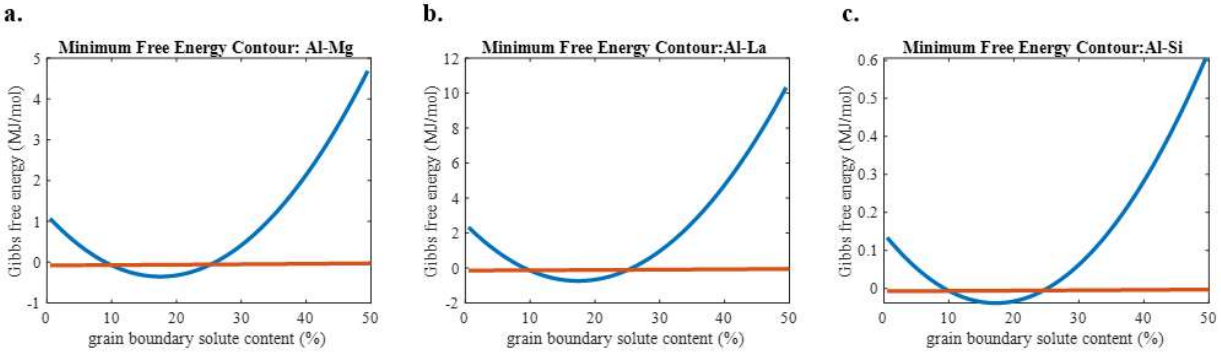

Figure 5. Gibbs free energy contours for Al-Mg, Al-La, Al-Si systems for a global solute content of $X = 0.2\%$.

nanocrystalline metal is reached. Binary nanocrystalline systems tend to exhibit rampant grain growth following second phase precipitation if the precipitate phase is energetically

favorable to one in which the material's alloying element is segregated to the material's grain boundaries. This effect is due to the precipitate phase consuming dopant atoms from the grain, which reduces its stabilizing effect on the microstructure. By this effect, precipitation of secondary phases due to the presence of dopants can disrupt the necessary segregation required for grain stability. This comparison can be seen visually in Figure 5 where the blue curve represents the nanocrystalline state, and the red curve represents the lowest energy state of the bulk large-grained microstructure and any precipitating phases. In the case that a precipitating phase is of a lower energy state than the nanocrystalline regime, the stabilizing solute in the material's grain boundary is utilized in the precipitation of the second phase, effectively reducing its presence in the grain boundary and thus its stabilization effect. As can be seen in Figure 5, for each chosen material system the free energy of the nanocrystalline state is lower than that of the bulk solution and any precipitating phases; this means that Al-Mg, Al-La, and Al-Si are stable against phase precipitation under dopant contents of 20%.

3.3. Influence of global dopant content on grain stabilization

The effect of varying global dopant content X on the free energy of a material system for the range of dopant contents most commonly used to synthesize binary nanocrystalline systems is shown in Figure 6(a); this range is chosen to promote stability without inciting secondary phase precipitation. It can be seen that a higher Mg dopant content, under the limit set by the onset of phase precipitation ($X \leq 13\%$), yields a higher degree of thermodynamic stability against grain growth. To this end, the optimal range of dopant content for each material system can be established. Within this optimal range, as shown by Fig. 6a, as global solute content is increased, so is the degree of segregation seen in the

material, as read by the grain boundary solute content value at which the minimum in the curve exists. It is intuitive to say the stability of the nanocrystalline structure will increase with an increase in the global dopant content. However, this apparently is not true as can be seen in Fig. 6b; although an increase in the global dopant increases the grain boundary content, it also leads to an increase in the free energy which trends the nanocrystalline system towards instability. When the concentration of the added dopant is in a supersaturated state in the nanocrystalline matrix, such thermodynamic conditions will promote second phase precipitates to nucleate and grow in the grain boundaries and grain interiors. Thus in NC Al-Mg, a global dopant content above 13% will be accompanied by the precipitatation secondary phases in the grain boundary region in order to reduce the free energy. Precipitation of secondary intermetallic phases can disrupt the necessary segregation required for grain stability.

Additionally, a material system's preference for the size of the solute atoms can be seen in Figure 6(b). From the results of the regular nanocrystalline solute model, a variation in solute atomic volume showed a two-regime effect; at grain boundary solute contents below 19% a large solute atomic volume resulted in a reduction in grain boundary energy presumably due to the large atoms' ability to reduce the grain boundary's free volume more effectively than small solute atoms. At grain boundary solute contents above 19%, small solute atomic volumes are preferred due to their lesser atomic misfit in the grain boundaries, and therefore lesser lattice strain effects. These lattice strain effects directly influence the material system's enthalpies of mixing and segregation as described in Eqs. (6) and (7), respectively. This concept suggests that comparing the atomic volumes of the

solvent and solute elements can indicate the propensity for the system in question to form a stable nanocrystalline state.

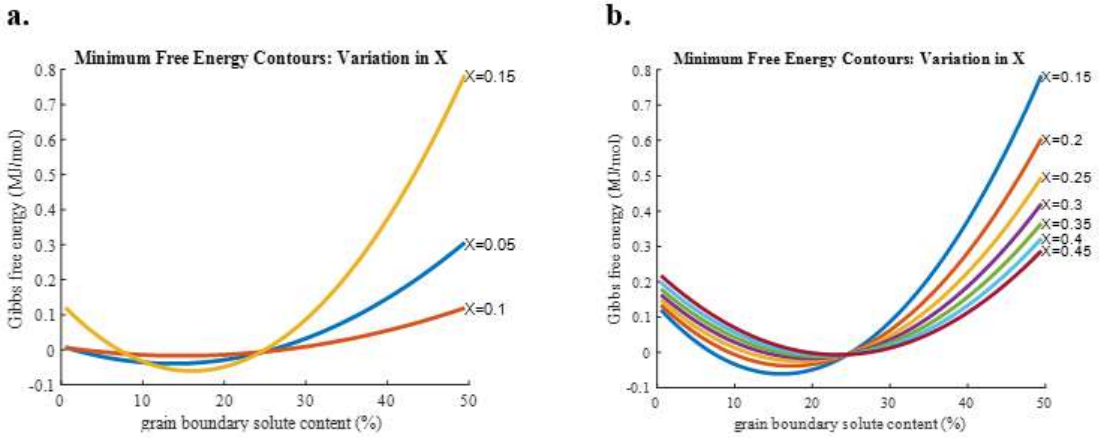

Figure 6. Influence of a variation in global Mg dopant content X on grain boundary stabilization in NC-Al (a) Mg dopant content in the dilute limit and (b) high Mg dopant content.

The thermodynamic effect of an addition of dopant excess (Γ) on grain boundary energy is described by the Gibbs adsorption isotherm

$$\gamma = \gamma_0 - \Gamma(\Delta H^{seg} + kTlnX) \qquad (11)$$

where γ is the reduced grain boundary energy as a result of solute segregation, γ_0 is the average grain boundary energy of the pure solvent material, ΔH^{seg} is the system's enthalpy of segregation, and X is the global dopant content [27]. The Gibbs adsorption isotherm predicts that as the degree of dopant segregation is increased, the resulting microstructure's final grain size becomes smaller. By varying the global dopant content in the nanocrystalline metal it can be shown that the model's free energy surfaces predict the effects of the Gibbs Adsorption Isotherm, Eq. (13), correctly; that is, as dopant content is increased, so is the content in the grain boundary, and therefore the final nanostructure's stable grain size is reduced as a function of solute excess. This relation provides a means for controlling the resultant microstructure of a manufacturing process in which a binary

nanocrystalline system is created. However, this control is limited in that no final nanostructure can be created with a final grain size smaller than that of the raw aluminum powder that is initially used in the process. The grain size is known to have a considerable influence of the material properties. The influence is efficiently described by the Hall-Petch relationship which follows

$$\Delta\tau \propto \frac{k}{d^x} \qquad (12)$$

$$\sigma_y = \sigma_0 + \frac{k_y}{\sqrt{d}} \qquad (13)$$

The Hall-Petch relationship predicts that the material's strength is inversely proportional to its grain size. This, in turn, by the commutative property, means that as the global dopant content is increased, so does the Hall-Petch effect's contribution towards the strength of the material. Additionally, as grain boundary segregation of dopant increases the excess free volume in the grain boundary is decreased. Therefore, the grain boundary's excess free energy is also decreased. By this mechanism, an increase in global solute content also increases the degree of stability of the nanocrystalline material, up to a limit set by the onset of phase precipitation at which point the precipitation of phases consumes dopants in the grain boundary reducing its stabilizing effect. In order to assess these effects, the free energy curves corresponding to an increase in global solute content were systematically created from the regular nanocrystalline regular solution model. While grain boundary solute content was varied throughout its full range, zero content to full saturation, the grain size was restricted by the breakdown of the Hall-Petch regime. Being that the regular nanocrystalline regular solution model is based on the assumptions of Hall-Petch, the model is only valid while those assumptions hold. According to Trelewicz [32], the Hall-

Petch regime begins to break down into a description of amorphous solids at a grain size of approximately 10 nm; as such, the model's grain size parameter was varied through the remainder of the nanocrystalline regime, 10 to 1000 nm. This breakdown is described by the Hall-Petch relationships of Eqs. (12) and (13), where σ_0 is the intercept value of stress from a material's empirically derived Hall-Petch plot, and k_y is the slope of the same curve

3.4. Empirical analysis of nanostructure stability

In order to analytically assess the stability of NC-Al against both grain growth and phase precipitation, an empirical stability criterion derived from the results of the regular nanocrystalline regular solution model was employed,

$$\frac{\Delta H_{seg}}{(\Delta H_{mix})^a} = c \qquad (14)$$

The parameters ΔH_{mix} and ΔH_{seg} which capture the thermodynamics of the grain interior and grain boundary environment were estimated for each NC-Al-dopant system using Eqs. (6) and (7), respectively. The criterion was calibrated using regression analysis of the original regular nanocrystalline regular solution model's stability predictions utilizing a large dataset of binary nanocrystalline alloys which yielded the fit coefficients a= 0.567 and $c = 4.425$ [33]. Since the dataset which was

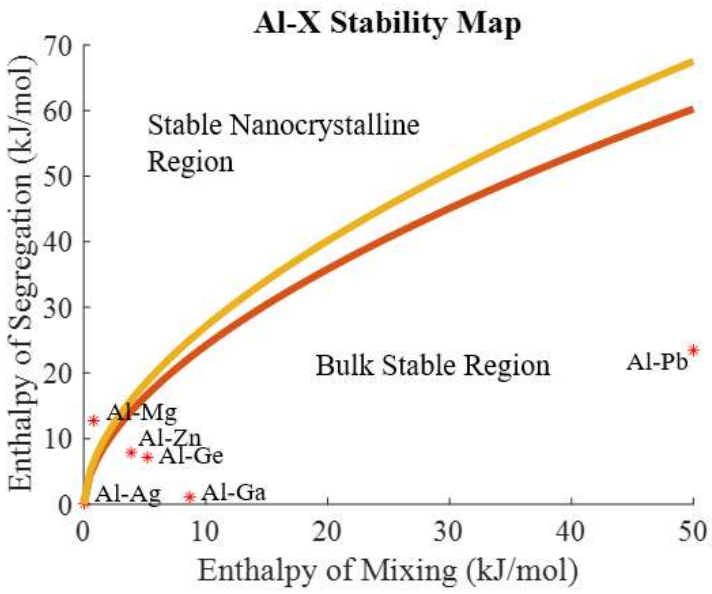

Figure 7. Empirical stability map for binary aluminum systems with positive enthalpy of mixing.

used was not restricted to aluminum solvents, the empirical stability criterion's predictions may exhibit systematic errors for aluminum systems due to uncertainties in the fit coefficients. The output of stability criterion Eq. (14) can be visualized in the form of a stability map that is characterized by the stable, metastable, and unstable regions separated by curves corresponding to an equal ratio between the enthalpy of segregation and the model's adjusted enthalpy of mixing.

The empirical stability criterion Eq. (14) was applied to each NC Al-dopant system to provide an additional source of data with which to reaffirm the predicted thermodynamically nanocrystalline states. The analysis was limited to NC Al-dopant systems with a positive ΔH_{mix}, which have a higher propensity to segregate to grain boundaries. According to the regular nanocrystalline regular solution criterion, solvent-dopant systems with sufficiently large enthalpies of segregation in relation to their model-adjusted enthalpy of mixing are predicted to be stable against both grain growth and phase precipitation. Figure 7 show a stability map for the NC Al-dopant systems which exhibit positive ΔH_{mix}. Three regions are present: the Bulk Stable Region where grain boundary segregation does not result in a stabilized nanocrystalline structure due to its free energy being greater than that of the bulk solution, the Metastable Region in which macroscopic phase separation would be preferential (despite the presence of a nanocrystalline state stable against grain growth), and the Stable Nanocrystalline Region for which the nanocrystalline state is stable against both grain growth and phase separation being that it is the lowest free energy state available. In order for a material to be chosen as a viable dopant for the purposes of this research, the resulting binary alloy must reside in the stable nanocrystalline region. As can be seen by Figure 7, the only binary system predicted to

exhibit this characteristic with a positive enthalpy of mixing is Al-Mg. As such, Mg has been identified as the most promising dopant to successfully stabilize nanocrystalline aluminum's microstructure. The empirical stability criterion's predictions are therefore consistent with observations from the free energy surfaces.

Additionally, by examining the material system's enthalpy of segregation and grain boundary interaction parameters it can be shown that there is a necessary minimum value in order for segregation to occur sufficiently to reduce the grain boundary energy to a level at which a stable nanocrystalline state is possible. This observation can be used as an additional tool to screen potential dopant elements and reaffirm the stability map's predictions; systems with increasingly negative values of the grain boundary interaction parameter exhibit the tendencies necessary to provide grain boundary stability.

4. Conclusion

The work described herein has been done in order to predict the dopant elements and their respective compositions for which nanocrystalline aluminum's grain size can be stabilized. The regular nanocrystalline solution model applied for binary nanocrystalline aluminum alloys predicts thermodynamic stability against grain growth and phase precipitation for Mg, La, and Si dopants. These dopants, when added to the material system above the required global dopant content for stability promote segregation to the grain boundaries resulting in a reduction in grain boundary energy. A global Mg content of 13% was found to promote the highest degree of stability in the binary Al-Mg nanocrystalline system. 10% La or Si content was necessary for stability, with higher contents corresponding to smaller final crystallize sizes without affecting the existence of a stable state. Additional dopant addition beyond this critical minimum global solute content results

in a characteristic reduction in average microstructure grain. These predictions can be used to inform which experimental materials shall best be created to facilitate investigations with the goal of establishing manufacturing techniques for bulk nanocrystalline aluminum alloys to be used in industrial applications such as power generation and transportation.

While the results derived from the modified Regular Nanocrystalline Solution model presented in this work are relatively reasonable, it must be noted that both the chemical and mechanical interaction terms of the model represent simplified dynamics corresponding to interactions based on bond energies and elastic effects only. As such, dynamic interactions such as atomic hysteresis effects have been neglected. Additionally, the enthalpies of mixing and segregation used in this work are subject to the limitations of Miedema's model. While these effects are expected to be small in terms of the results presented herein, in some cases deviation between experimental and modeled results is to be expected.

II. Paper 2

Deformation Mechanisms in Nanocrystalline Al-Mg

Jake Hohl[1], Leslie T Mushongera[1,*]

[1]Department of Chemical & Materials Engineering, University of Nevada, Reno, Reno, NV, 87557, USA
**Corresponding author: lmushongera@unr.edu*

Abstract

Thermodynamically stabilized nanocrystalline alloys exhibit increased strengths and reduced ductility relative to their coarse-grained counterparts. In order to illuminate the mechanisms by which these materials deform, and thereby inform manufacturing methods of the bulk materials, molecular dynamics studies were conducted for Al-Mg (10%) in uniaxial tension for periodically bounded material sections. Voronoi tessellation was used to initialize the microstructure while Molecular Dynamics was used to simulate thermodynamically driven dopant segregation and uniaxial tension. It was found that grain boundary mediated deformation dominated the microstructure, with interfacial cracking occurring as a primary mode of material failure.

1. Introduction

Due to the small average crystallite sizes of nanocrystalline microstructures, their deformation mechanisms are expected to significantly deviate from their microcrystalline counterparts. Specifically, a transition from slip mediated deformation to grain boundary interface mediated processes is expected with the onset of the nanocrystalline regime.

The onset of this regime is expected to occur around 20-40 nm average crystallite size, determined by a balance in dislocation source stress and the shear strength of the material. At this crystallite size, down to a limit determined by the breakdown of the Hall-Petch regime below ~10 nm, material strength increases as crystallite size decreases [32]. This effect in nanocrystalline metals is typically attributed to a decrease in dislocation mobility due to the impediment to their motion provided by the high volume-fraction of disordered high energy grain boundaries in the material [34,35].

In this new regime, grain boundary deformation processes are expected to be limited to grain boundary sliding, rotation, and annihilation. This grain boundary annihilation and migration is the primary mechanism by which crystallites coalesce and the material undergoes grain enlargement [36]. However, the nanocrystalline Aluminum stabilized by Magnesium studied in this work is expected to be thermodynamically stable against this grain enlargement mechanism [37]. To this end, this work discusses the remaining two mechanisms as well as grain boundary cracking, dislocation pile-up and layering, and the mechanism of grain boundary expansion and volumetric strain, which in the stabilized nanocrystalline material replaces that of grain boundary annihilation. In this work the hypothesis that the replacement of grain boundary migration with grain boundary enlargement and straining is caused by the suppression mechanisms of the dopant material, in this case Magnesium, is supported by Molecular Dynamics simulation.

Understanding and controlling these mechanisms may provide a pathway for increasing the limited ductility and fracture toughness inherent to these materials [38]. The most effective way of controlling these properties, and the stable grain size of the

material's microstructure, is shown to be controlling the content of the dopant element added to the base nanocrystalline metal. This effect on grain expansion is investigated in this research, while the effect on the stable grain size is investigated in prior research by the authors [37].

2. Methodology

In order to assess deformation mechanisms in NC Al-Mg, Molecular Dynamics simulations were conducted through the use of the LAMMPS code on the University of Nevada, Reno high performance computing cluster, Pronghorn. Atomsk was employed for microstructure initialization and Ovito was utilized for visualizations.

Simulated nanocrystalline Al-Mg(10%) microstructures were initialized by the use of stochastic Voronoi tessellation with an initial average crystallite size of 10 nm. To do this, crystallite nucleation sites were initiated on nodes at the required average spacing of 10 nm. A tolerance of 0.5 nm was accepted in relative positioning. The absolute position of each node was determined stochastically in the simulation region, consisting of a 200 nm by 200 nm cell. Grain boundaries were then drawn at the intersecting regions of each node's surrounding space and crystallites were nucleated in these interiors. In this way, 20 3-D grains were formed in the simulation volume. By using a periodically bounded material section, the given simulation volume can be considered as a portion of a bulk material. As such, results of the model should generalize to experimentally synthesized materials.

Magnesium segregation to the grain boundaries of the Aluminum microstructure was simulated by resolving forces and potentials between the dopant Mg atoms and both the crystallite Al and grain

boundary Al atoms numerically. Magnesium's low mixing enthalpy and high segregation enthalpy when placed in Aluminum provides the driving force for Mg to migrate to grain boundary sites in the nanocrystalline Al. Partitioning of the dopant in the material is resolved during Molecular Dynamics simulation from the empirical interatomic potentials used in the simulation.

Strain controlled uniaxial tension was then applied to the resultant microstructure at a strain rate of 1E-5/sec. During the simulated test, atomic motion was resolved through the use of the empirical potential and utilized to track the motion of both Al and Mg atoms under loading. Additionally, mechanical response and the classification of atoms as Al, Mg, intercrystalline, grain boundary, and dislocation were used to track changes in the microstructure, namely volumetric strains of each region of the microstructure as well as dislocation motion.

3. Discussion and Results

To investigate the dominant mechanisms of deformation in nanocrystalline alloys, a simulated microstructure of 10 nm average grain size consisting of 90% Aluminum and 10% Magnesium dopant was initiated and evolved to its segregated state, with the

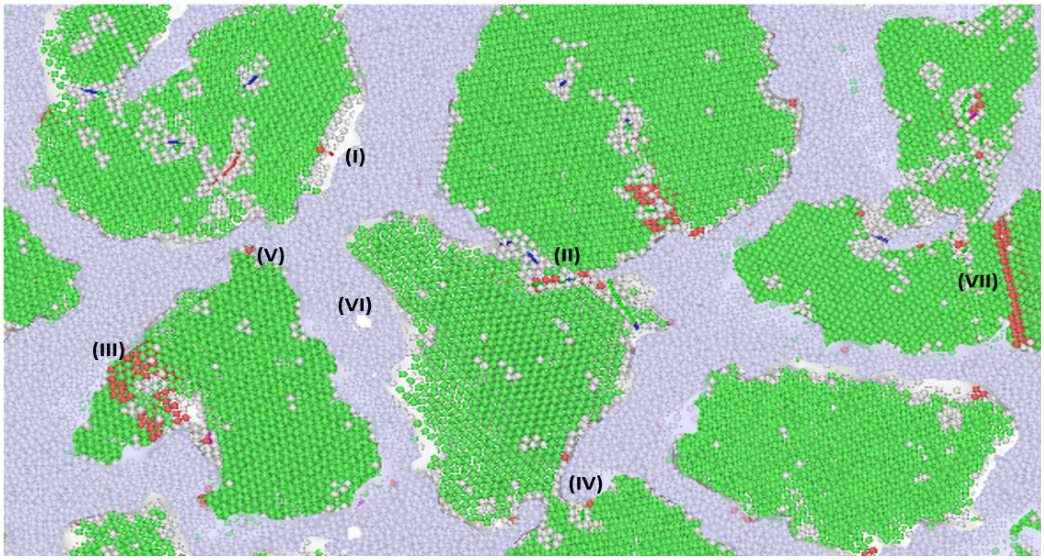

Figure 1. Summary of Molecular Dynamics simulations of nanocrystalline Al-Mg deformation mechanisms. (I) grain boundary interface cracking (II) grain boundary dissociation (III) twin deformation (IV) grain boundary interface curvature effects (V) interface dislocation nucleation site (VI) grain boundary void formation (VII) dislocation.

majority of the Magnesium dopant residing at the material's grain boundary. A uniaxial tension test was then simulated according to ASTM standard E8. The resulting microstructure, shown in Figure 1, was then analyzed according to its deformation and atomic displacement state, alongside the microstructural evolution under loading as tracked throughout the numerical time-steps of the simulation. It was found that grain boundary interface mediated deformation mechanisms dominated the microstructure, with interfacial microcracking (I in Figure 1) occurring as a primary failure mechanism.

Grain boundary dissociation, twin deformation, interface curvature cracking, void formation, and dislocation layering were also found in the microstructure as seen in Figure 1. These effects are a combination of the dominant mechanisms in nanocrystalline materials and dominant mechanisms typically found in microcrystalline materials (to a lesser degree). This suggests that as nanocrystalline grain boundary mediated mechanisms begin to dominate the microstructure they do suppress the occurrence of slip-based deformation mechanisms but do not entirely arrest their existence. It also can be seen from (II) in Figure 1 and from the detail view in Figure 2 that grain boundary dissociation can occur as a combination of a typical nanocrystalline mechanism and microcrystalline mechanism. In this case, grain boundary interface cracking as a result of high interface curvature interacts with dislocation slip at the grain boundary causing the boundary to break down and two grains to coalesce. In this study, this is the only mechanism that is able to surmount the stabilization effect of the Mg dopant against grain enlargement. This result suggests that, in order to further avoid grain enlargement in the stabilized microstructure high interface curvatures at thin grain-boundary regions near possible dislocation nucleation sites should be avoided. While direct control of this scenario is not practical in

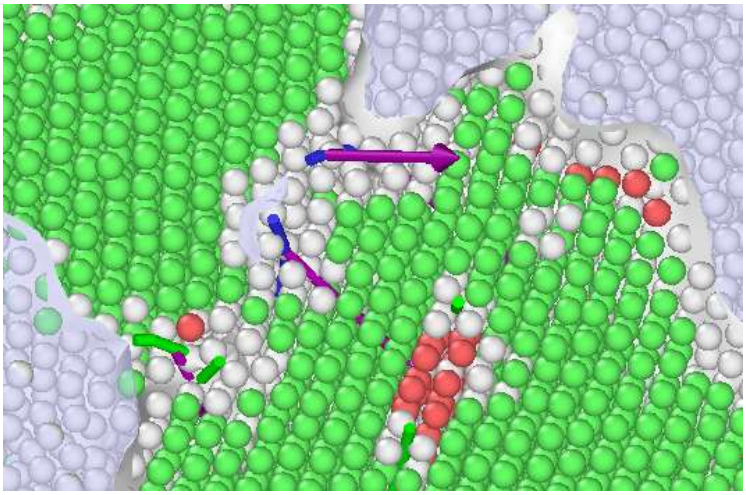

Figure 2. Grain boundary dissociation mechanism, dislocations along the grain boundary with orthogonal Burgers vectors (purple).

experimental materials, the observation serves to provide evidence that a high degree of uniformity in the microstructure, created during the grain refinement process, is very desirable.

Furthermore, it can be seen from (I) and (IV) in Figure 1 that interface cracking (Figure 3) and void formation (Figure 4) in the grain boundary region are primary deformation mechanisms that are significantly more prominent in the nanocrystalline state. This study has found that interfacial cracking, a dominant failure mechanism in the material, occurs by two primary mechanisms: cracking in the wake of atomic flow (I), and cracking at interface impingements of the atoms (II). Wake crack formation occurs when atoms flow away from an interface. Because of a mismatch in the atomic flow rates in the crystalline interior and the grain boundary region, as the

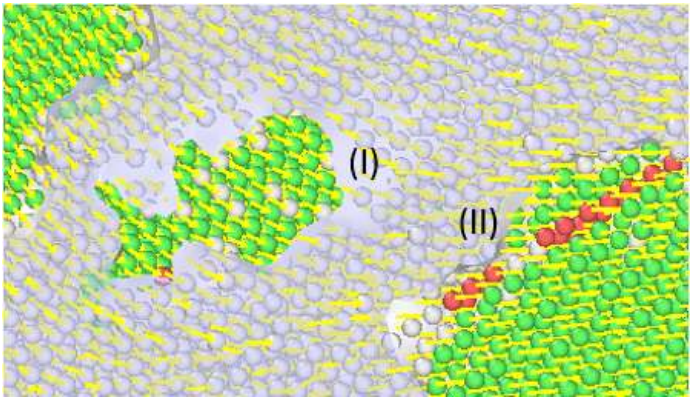

Figure 3. Grain boundary atomic motion effect on interface cracking (I) crack forming in the wake of atomic flow (II) crack forming at interface impingement.

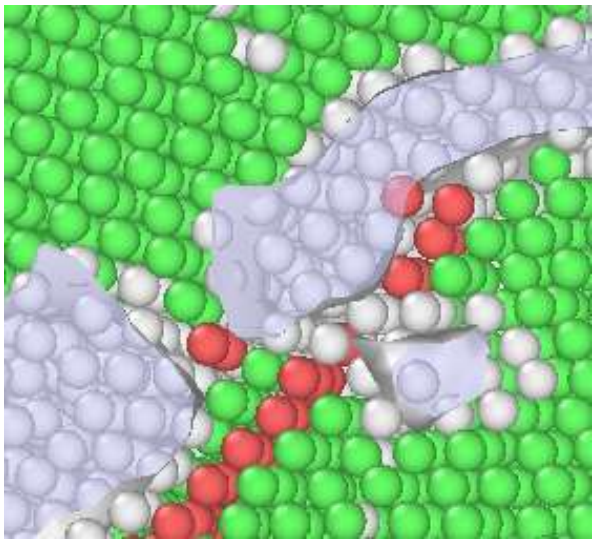

Figure 4. Void formation, dislocations close off a portion of the crystallite interior which forms an internal void.

displacements increase in the grain boundary region the atoms are pulled away from the interface forming an elongated crack. Impingement cracking occurs when these atoms flow into an interface, as they atoms contact the interface at a higher velocity and displacement than can be accommodated in the crystallite interior region they form a pile-up and resulting localized crack. The effects resulting from these mechanisms may be identified as the cause of the reduced ductility in the material due to its high volume fraction of grain boundaries; they may also be exacerbated by the reduced grain boundary mobility provided by the stabilizing Mg dopant. To this end, these effects may be the driving force for the inherent trade-off in strength, stability, and ductility, in this material. As of yet, a controlling mechanism for this set of deformation mechanisms has not been identified, but from knowledge of crack initiation and fracture mechanics it can be hypothesized that a high degree of surface finish control may reduce crack initiation. Also, matching volumetric strain rates between the composition of the crystalline interior and grain boundaries would serve to decrease the interface cracking effect significantly as the crack forms from a mismatch in deformation rates between the two regions under loading.

It can be also seen from the dispersion of dislocation nucleation sites (V in Figure 1) that the primary nucleation location is at the grain boundary interface. From (VII in Figure 1) and the detail view in Figure

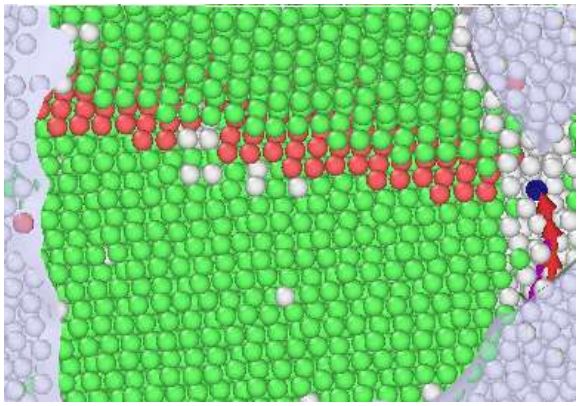

Figure 5. Dislocation layering and localized slip.

5 it can be seen that these dislocations then form a front and propagate across the crystallite interior forming a layering effect. This semi slip-based deformation mechanism may be the nanocrystalline equivalent of traditional dislocation propagation and slip seen in microcrystalline materials. From a simple review of the microstructure it is noted that the scenario occurs much less frequently in the nanocrystalline microstructure than the traditional microcrystalline case. This result reinforces the suppression of slip-based deformation processes in these materials.

Figure 6 details a surface view of the atomic motion on a microstructural plane parallel to the applied tensile load. From the figure, it can be seen that the atomic flow is generally uni-direction in the crystallite interiors; conversely, atomic flow in the grain boundary regions has a distinct curvature driven by the large-scale interface curvature in its local region. It can be hypothesized that this effect is due to the lack of accommodation of the high displacements of atoms in the grain boundary region relative to lower displacements in the crystallite region, this mismatch forces the grain boundary atoms to follow the path of least resistance and re-direct their motion into the direction of the grain boundaries. This atomic flow enables the

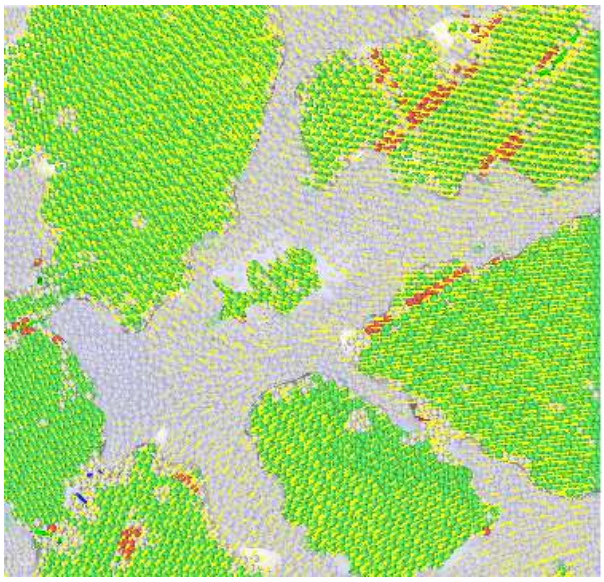

Figure 6. Atomic flow, direction of applied load. Atomic displacement is denoted by yellow vectors.

aforementioned mechanisms of both interfacial cracking by the wake mechanism and impingement mechanism as well as void formation in the crystallite region at the interfaces of the grain boundary.

It was found, by molecular dynamics and confirmed by review of experimentation by other research groups, that the exhibited ductility of the material is strain rate dependent. A roughly linear relationship has been found between an increase in strain rate and a corresponding increase in ductility for nanocrystalline tensile tests. This phenomenon may be attributed to an increased kinetic energy of dislocation flow allowing individual dislocations to more easily surmount energetic barriers, namely

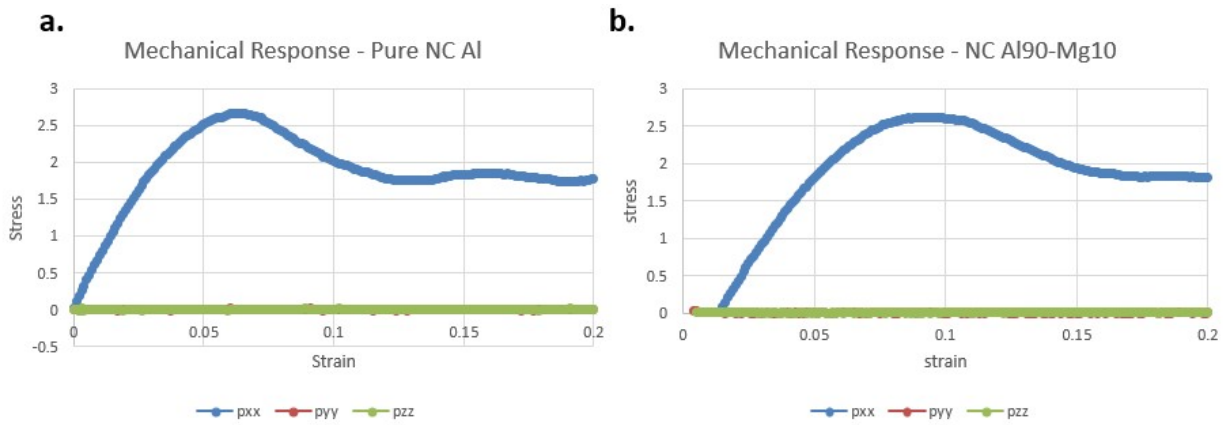

Figure 7. Mechanical response under tension (a) pure nanocrystalline Al (b) nanocrystalline Al-Mg(10%).

disordered grain boundaries. To this end, dislocation mobility is increased, and dislocation pileup is decreased, in the material. Being that higher ductility corresponds to increased dislocation mobility, this coupled effect leads to higher effective ductility in the material. Conversely, as Magnesium dopant is added to the material and segregated to the grain boundaries Zener pinning effects increase proportionally with the amount of

segregated dopant. This effect serves to arrest grain boundary mobility and increase dislocation pileup, leading to increased material strength at the expense of ductility, as can be seen in Figure 7. These effects provide a means by which the strength and ductility can be balanced indirectly by direct control of the material's composition.

Furthermore, by tracking the components of the microstructure throughout the simulated tensile test, a characteristic increase in the volume fraction of the material's grain boundary was observed alongside an accommodating decrease in the volume

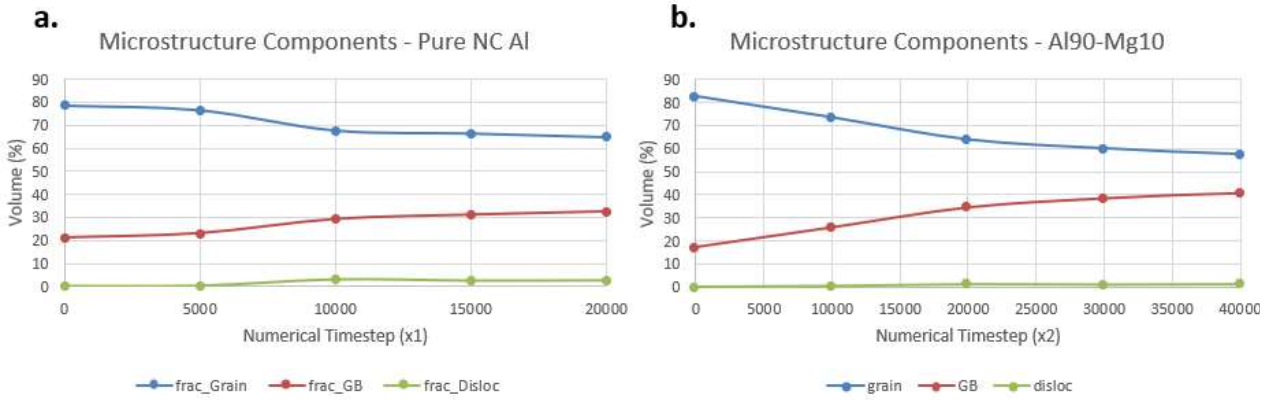

Figure 8. Components of the microstructure by volume (a) pure nanocrystalline Al (b) nanocrystalline Al-Mg(10%).

fraction of the material's crystallite region as seen in Figure 8. This strain-based grain boundary enlargement effect indicates that the grain boundaries of the nanocrystalline material are resisting a disproportionately high fraction of the load on the material thereby strengthening the material during deformation. This effect may explain the strain hardening effects seen in Figure 8. Being that the Magnesium doped nanocrystalline Aluminum exhibits a higher degree of both grain boundary volume fraction increase and strain hardening relative to the simulated pure nanocrystalline Aluminum, it can be said that the addition of the dopant element increases the proportion of the load that is taken

by the grain boundaries of the material relative to its grain. This is consistent with the idea that the Zenner pinning effects of the added dopants serve to strengthen the grain boundaries of the materials by arresting their motion.

4. Conclusion

Molecular Dynamics studies of nanocrystalline Al-Mg(10%) metallic alloy elucidated the deformation mechanisms that begin to dominate the material's thermodynamically stabilized microstructure as grain boundary mediated deformation processes overtake and suppress slip mediated deformation. It was found that the stabilization against grain enlargement provided by dopant Mg caused the typically prominent nanocrystalline deformation mechanism of grain boundary migration to transition into grain boundary straining and accommodation. Additionally, grain boundary interface cracking due to a difference in deformation rate between the crystallite interior and grain boundary was found to be a primary mode of failure in the material.

III. Paper 3

Microstructure Feature Recognition by Convolutional Neural Network

Jacob Hohl*, Leslie T Mushongera*

Department of Chemical & Materials Engineering, University of Nevada, Reno, Reno, NV, 87557, USA
**Corresponding authors: lmushongera@unr.edu, jhohl@unr.edu*

Abstract – Identifying features of importance in both simulated and experimental material samples has traditionally been a manual task performed through a researcher's experience and comparison to prior analyses. An automated system based on machine learning, specifically a Convolutional Neural Network, alongside image processing techniques was used to automatically identify and label prominent features of a material's microstructure. The algorithm was developed as an enclosed system encompassing the entire data pipeline that can be used as a black box. Simulation or test data, in the form of a single 2-D image, video feed, or 3-D volume is taken as input, and classified images are given as output. This design facilitates the use of the computational framework by a diverse user group, including those who are not trained in materials engineering or machine learning. The framework's performance was tested and validated through the use of a dataset comprised of simulated nanocrystalline Al-5 at.% Mg atomistic data. A classification accuracy of 90% across the test dataset was achieved with adequate computational efficiency.

1. Introduction

Identifying features of a simulated or synthesized material microstructure is of primary importance to the analysis of potential material failure modes, and of post-mortem failure analysis. Traditionally this task has been done qualitatively through inspection by a trained individual. This task, performed manually, has proven to be a challenging and repetitive task subject to large variances in classification accuracy depending on the experience of the researcher. Additionally, the classification task has been found to be extremely time consuming. By automating the task such that only an initial dataset must be labeled for training a deep learning framework the time and associated cost of this labor can be exponentially reduced.

Automation of this task, through the use of a machine learning system, may serve to greatly reduce analysis time and the requirement of expertise in the field. As such, a production system of this nature is of extreme value to multi-disciplinary researchers and industry alike. Current applications of machine learning models for materials science have included electrical and crystal property predictions based on visual feed data, as well as mapping relationships between numerical input data and numerically represented material properties [references]. As of yet, no complete frameworks designed to classify the features of material microstructures with adaptability to both simulated and experimentally created images as well as video feed data have been presented. Traditionally microstructure feature recognition has been automated by the use of expert systems based on segmentation of the visual field. Initially, these frameworks primarily consisted of digital image processing techniques which segment microstructural images into regions of interest that are then analyzed further through comparisons to other image datasets [39]. However, the main drawback of these algorithms is that they are prone to segmenting along an improper length

scale causing features to be either disjointed or outscaled such that they are not accurately represented. Additionally, while images of features of interest are created by these algorithms, they cannot be automatically classified by the algorithm. As such, manual classification is still required by the researcher.

Additionally, Support Vector Machines (SVM) have been employed to compare microstructure image signatures, generated through processing steps, to those of labeled data in order to perform the classification task [40]. An accuracy of approximately 80% has been achieved with such systems. Deep learning classification systems for microstructural data have also been previously proposed. These systems are typically pixel based approaches, as opposed to object based approaches such as the framework represented in this paper [41]. Pixel based approaches have the advantage of somewhat higher classification accuracy at the expense of an increase in computational cost. The approach presented in this paper favors the object-based approach with additional network layers and additional image processing steps in order to achieve comparable accuracy at less computational cost. As a result of this, larger datasets may be effectively classified. Transfer learning approaches have also been proposed for microstructure image classification by deep learning with the benefit of increased generality and adaptability, at the cost of varying accuracy [42]. This approach is a time efficient way to perform the classification task over a large variety of datasets with little to no algorithm modification and no network retraining, but generally suffer decreased performance relative to specified frameworks that retrain on a dataset specific basis, such as the framework presented here.

In this work, and object-based CNN utilizing a dropout operator and numerically encoded image data was employed in order to develop a computational framework capable

of generalizing across multiple input data formats and material classes to identify and classify relevant microstructural features. Through the approach described herein generality is achieved while retaining high accuracy at relatively low computational cost. In the test case of this paper, we present simulated microstructural images, generated through modified Voronoi tessellation, of nanocrystalline Al-5 at.% Mg in its segregated state such that the dopant element Mg resides primarily at the material's grain boundary, serving to stabilize its microstructure. Evolution of the microstructures under loading was evaluated through Molecular Dynamics simulated uniaxial tensile tests in order to assess the plasticity response of the material under load. The simulation parameters and workflow were modeled off of previous analyses conducted by the authors [43]. The automated feature recognition framework proposed in this work sets the methodology for further material studies regarding hypothesis formulation from the aggregate data that can be generated. To this end, the work herein facilitates rapid development in the field of nanocrystalline metal alloys, and potentially other classes of materials.

Section 2 will provide some background on CNNs in general, as well as the specific implementation and data representation used in this study. Section 3 will introduce the data sets on which the computational framework was validated. The results of this evaluation, as well as an investigation regarding the classification accuracy of the algorithm is presented in Section 4. Finally, conclusions and next steps are discussed in Section 5.

2. Framework Structure

Convolutional Neural Networks are a subset of feed-forward deep neural networks used to classify images. These algorithms work by using fully connected layers of perceptrons

that optimize their loss function by systematically passing filters over processed images and propagating information forward through these layers [44,45]. This classification process is primary accomplished through the recognition of feature edges and their orientation; this is done by the activation of neurons that are activated solely by the presence of these edges, and that are specific to their orientation. By tracking the state of the filter and the activation of these neurons, the presence and location, as well as orientation, of the edges in an image can be identified. The patterns of these edges in their encoded images as well as these patterns' relationships to pre-defined class labels can be learned by the model in order to form the classification schema [46]. In this way, patterns in labeled image data can be learned and applied generally across datasets.

2.1 Components of the Framework: The computational framework was established to be modular and adaptable by sub-sectioning the overall task into three sub-tasks, microstructure creation, image pre-processing, and feature recognition as seen in Figure 1. As such, the algorithm is presented in such a way that it is general across any material class for which microstructural image data can be generated with only changes to the hyperparameters used in the neural network in order to account for longer or shorter convergence times depending on the complexity of the classification task.

Parameters of the material to be studied, including composition and morphology, as well as seeding parameters for microstructure simulation are specified at the onset of the study in order to fully define the initial microstructure to be studied. Once the parameters of the studied material are defined, Voronoi Tessellation performed through the Atomsk code set is used to systematically structure the requested microstructure. This process is performed by randomly linking randomly systematically dispersed nodes at the specified

spacing, determined by the length scale of the microstructure in question. From these nodes the contours of the grain boundaries are defined, atom seeds are nucleated at the node sites, and truncated at the grain boundaries. In this way, an initial polycrystalline structure is formed.

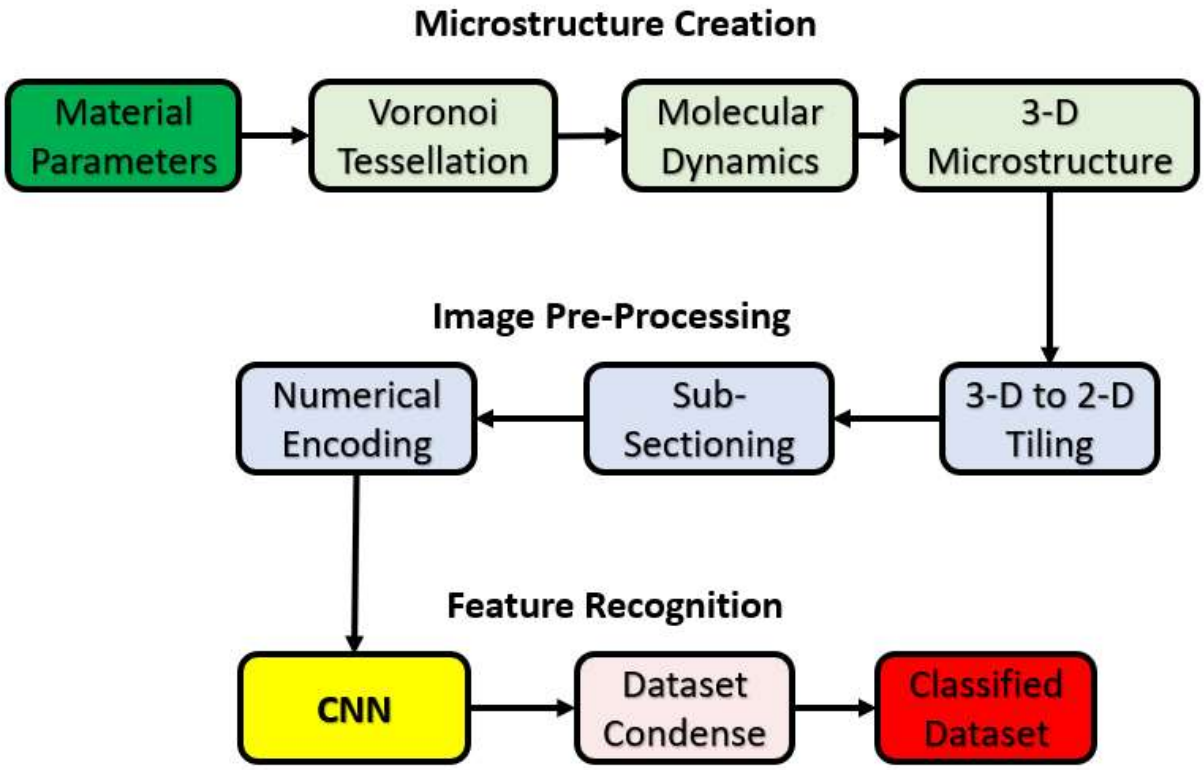

Figure 1. Computational framework structure, sub-sectioned into three tasks: microstructure creation, image pre-processing, and feature recognition. Holistically these components map input image data to classification labels as output.

From this initial microstructure, in the case of an alloyed and segregated nanocrystalline material, Molecular Dynamics performed by the LAMMPS code set is done to simulate thermodynamic segregation of dopant (in this case Mg) atoms to the grain boundaries of the initial pure nanocrystalline aluminum structure. From this process the distribution of the dopant element is determined. The segregated microstructure is then used as the test

sample for a simulated tensile test, also driven by Molecular Dynamics simulation and the LAMMPS code. Uniaxial tension is applied to the simulated specimen at a given strain rate (ASTM standard here) and duration. This simulation serves to resolve the redistribution and deformation of the Aluminum nanocrystalline grains, the amorphous grain boundary structure, and the Magnesium dopant elements.

The generated 3-D microstructure must be processed into numerical data for compatibility with the CNN. In order to do this, and to increase computational efficiency of the framework, the 3-D microstructure is sub-sectioned into 2-D slices and tiled into a single image of larger dimensions than the initial microstructure. This tiled image is then sub-sectioned onto the length scale of interest, driven by the average size of the microstructural features of interest. These images are then converted into 256 color scale palletted image data and numerically encoded into 2-D matrices, which are then stacked into a 3-D matrix with each layer of the 3rd dimension corresponding to an individual image. Each index in the 2-D matrices correspond to a pixel location in the original image, with the value of the cell corresponding to a single-color shade of the 256 total possible colors. In this way the image data is prepared for use by the CNN.

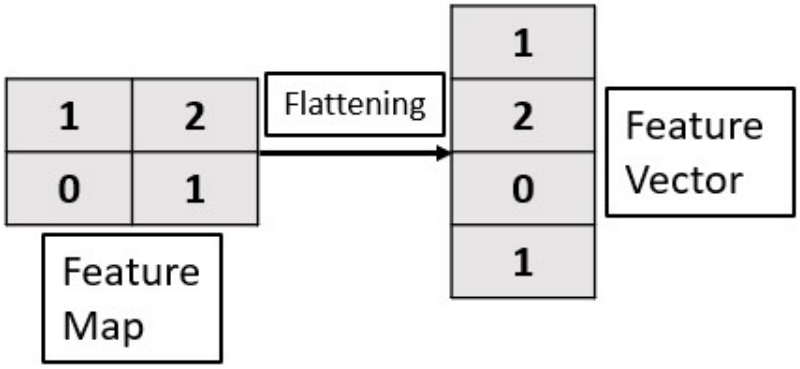

Figure 2. Flattening Layer, utilized by the CNN used to format the feature map for use by the final classification step of the algorithm, the output layer.

The feature recognition task is performed through the use of a CNN, described in detail in section 2.3 and 2.4. This algorithm utilizes labeled and processed image data in order to

learn a classification relationship that is then used to label further microstructure images. The output of the CNN is a set of labeled matrices corresponding to microstructural images. This data is condensed by converting the numerical data back into Red-Blue-Green (RGB) color scale images. These images are then tiled back onto the dimensions of the original input data in their original order, effectively recreating the original dataset albeit with included labels. This final dataset forms the end result of the CNN, a classified image dataset of the original form.

2.2 Components of the CNN: Convolution network layers quantify and reduce image field data in order to systematically recognize patterns in the input image data. They work by passing a kernel matrix over the image in a repeatable sequence and computing the dot product between the visual field's numerical data in a specific region and the weights of the kernel; the resultant scalar computed quantity describes the activation of the network's neurons in the form of a feature map. This feature map can then be passed through an activation function used to represent the visual patterns that each region of the image exhibits. The types of kernel, defined by the values of the kernel matrix, dictate the types of features that are recognized by their use. In order to identify all of the

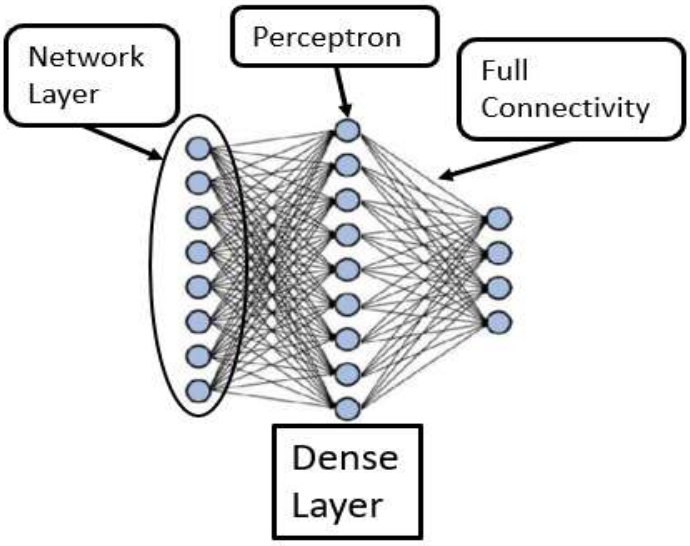

Figure 3. Dense Layer, used to facilitate the final classification step of the algorithm, and provide full connectivity of the network layers.

features of interest in an image, multiple kernels and therefore feature maps are typically necessary. The values of the kernels are the weights of the network that must be learned during the training process to encode the classification relationship, IE the mapping between input data and extracted features [46,47]. This learned relationship forms the core of the algorithm by which the classification task is achieved.

Subsampling is done in order to reduce overfitting of the model by reducing the dimensions of the input data. This is done by a variety of algorithms, the most popular of which is max pooling. Max pooling reduces the area of the image currently covered by a kernel to the largest value in that 2-D area. This process essentially reduces the occurrence of small-scale intricate features in favor of more influential large scale image features of lower effective image resolution [44,46,47]. This results in a more generalized classification relationship while retaining the overall accuracy of the algorithm.

Dropout layers were added to the model in order to reduce overfitting. This layer works

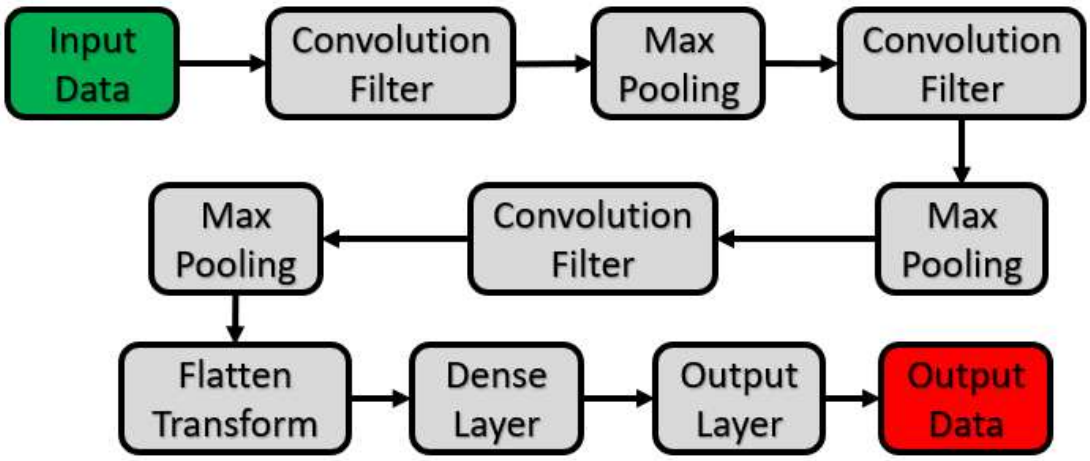

Figure 4. Detail of the CNN's structure. Operations used to map the input data to output data are shown as well as their connectivity.

by randomly dropping outputs of the preceding layer at a probability specified by a

hyperparameter. This effectively reduces the model's ability to memorize dataset patterns such that adaptability is lost, thereby increasing the generality of the model [44]. Once the CNN has arrived at a pooled feature map a flattening layer, shown in Fig. 2, is used to reduce the dimensionality of the feature map from 2-D to a 1-D feature vector to be used as input for the final classification step, the output layer. In order to facilitate this classification, a dense layer, shown in Fig. 3, is used to provide full connectivity through vector multiplication for the final classifier, and to create class scores from the network's activations [46,47]. This operation forms the final step of the classification task.

The CNN's output layer is used to transform the input from the previous dense layer into labeled classes. In this way, the result of the algorithm is aggregated and presented in the correct format of image labels tied to image data in order to form a classified pair, at this step the algorithm is complete.

2.3 CNN Structure: The Convolutional Neural Network is structured by fully connecting multiple convolutional and subsampling network layers alongside multiple kernels for feature recognition as seen in Fig. 4. These layers are stacked, output to input, such that each subsequent layer learns higher level features in the data. Additionally, multiple kernels corresponding to multiple features are processed in parallel over the input image data. As such, the parallelized and connected algorithm is computationally efficient and capable of learning complex feature relationships from a relatively simple network structure. The patterned structure of convolution layers tied to max pooling layers is the means by which higher level features are learned in subsequent network layers. By using max pooling to reduce the dimensionality of the data low level features are lost while high level features are brought to prominence.

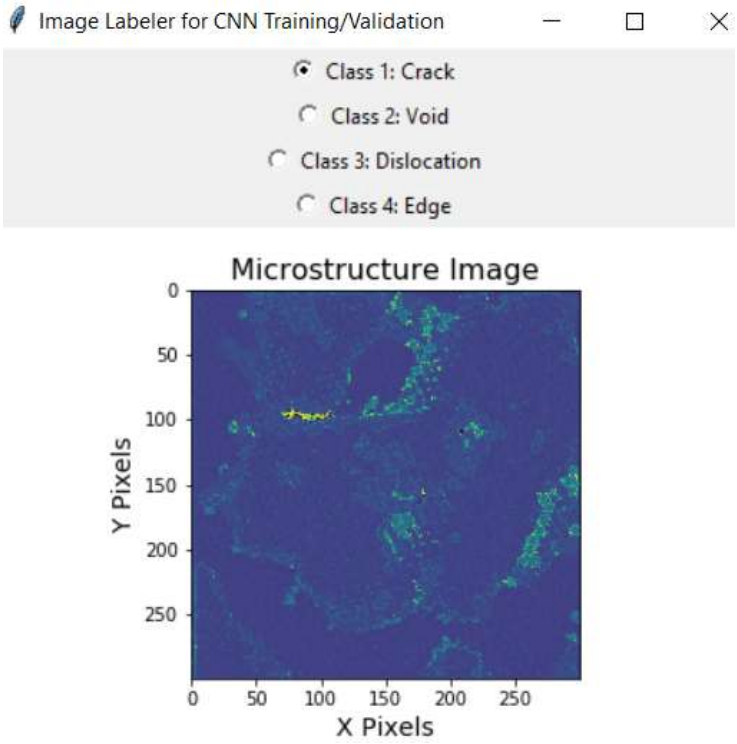

Figure 5. Model interface implemented in Tkinter, used to label image data for training of the algorithm.

3. Implementation

For the purpose of microstructure feature recognition, a Convolutional Neural Network was implemented in Python through the Keras Application Programming Interface (API) and used in conjunction with Pillow's imaging library and accessed via a Tkinter interface. The algorithm's interface (Fig. 5) provides a systematic means of training the CNN through image labeling. Microstructural images are presented to the user who is then prompted to label them according to pre-defined classes. These data are then stored in numerical format and passed to the main algorithm for use as train/test data to both form the labeling pattern and test its efficacy.

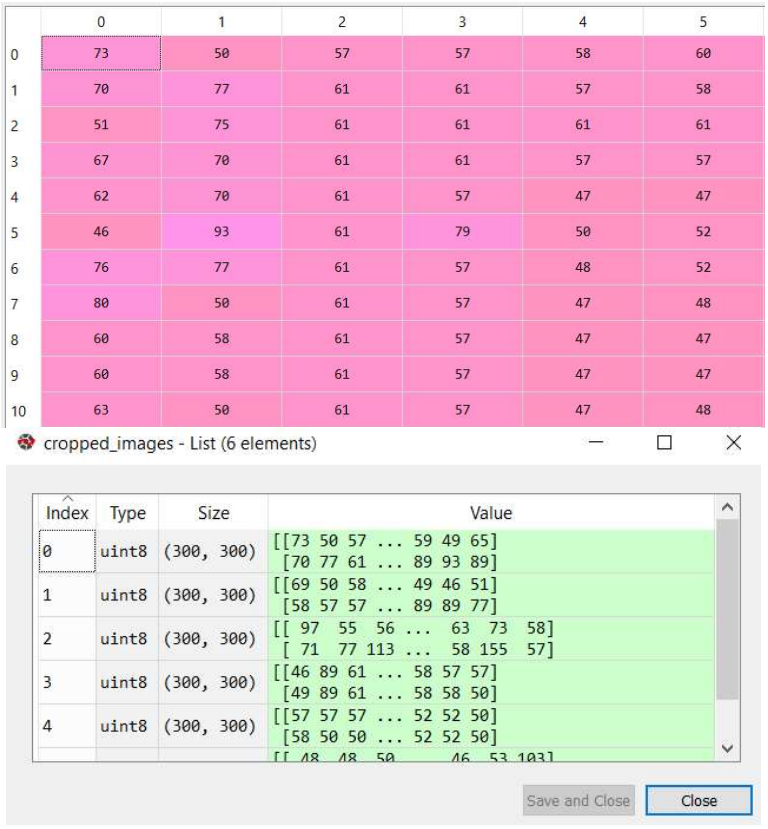

Figure 6. Input data format, numerically encoded image data represented as a 256 palleted color scale pixel array.

The algorithm accepts data in the format of a single 2-D image, or 3-D image sliced and tiled into 2-D. The input image is then sub sectioned and rescaled into multiple images of the length scale of the microstructural features of interest. These images are then converted into numerical palleted 256 color scale data in the form of a matrix, an example of which is shown in Fig. 6, where each cell represents an individual pixel location, and the cell's

numerical value corresponds to one of the 256 colors in the pallet. This data can then be processed by the CNN.

Class labels, derived from the labeling process done through the algorithm's interface, are then converted to one-hot encoding of appropriate shape to match the length of the image data. These data are then concatenated and associated into pairs of image and label. The pairs can then be split into training and testing data in an 80%-20% ratio respectively. This process can be replicated by the algorithm for the analysis of video feed data. By taking frame-by-frame images and sub-sectioning them onto the appropriate length scale a set of 2-D images can be created and utilized by the analysis framework. This adaptation of the algorithm is valuable in that it can provide automated analysis of video data captured during mechanical testing of material specimens which allows for tracking of microstructural evolution under loading.

The CNN was implemented through the use of the Keras API. The sequential model was manually structured through the addition and definition of each network layer. A 13-layer network was employed with 356,234 trainable parameters comprised of convolution layers, LeakyReLU activation functions, and max pooling and dropout operators. Due to the full connectivity of the network's layers, the CNN algorithm is prone to overfitting. In order to avoid this problem, the Leaky Rectified Linear Unit activation function was used to improve gradient flow and avoid the problem of dying Rectified Linear Units [48]. This solution allows for the detection of inter-related decision boundaries, allowing for the delineation of related classes. Additionally, the network structure was chosen through an iterative study utilized to optimize the classification ability of the network while avoiding model overfitting. This performance was ensured by randomly varying the training and

testing data to assess adaptability of the classification paradigm. The results of the algorithm are presented by outputting the test images alongside their assigned class labels, defined in the training process, and predicted class labels, derived from the CNN algorithm. The accuracy of the CNN's labeling schema is then calculated as a ratio of correctly labeled images to the number of total test images.

4. Results and Discussion

A sample case corresponding to the decomposition of a 903 by 608 pixel 2-D Molecular Dynamics simulated microstructure (Fig. 7) of nanocrystalline Al-5 at.% Mg was used for model validation. This decomposition, performed by the algorithm's interface back-end,

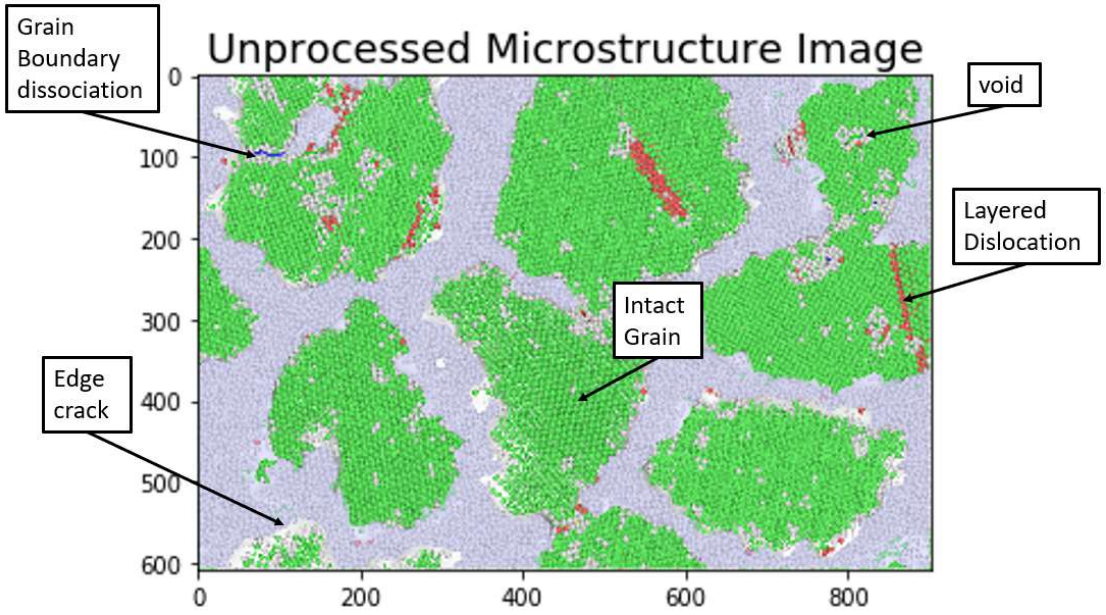

Figure 7. Simulated microstructure image data produced by Voronoi Tessellation coupled to Molecular Dynamics.

resulted in 208 50 by 50 pixel images, encoded into 256 color palleted numerical data, represented in the form of a list of Numpy nd-arrays where each element in the list corresponds to a single image. These images were then labeled manually through the

interface described in section 3. This pairing of numerically encoded image data, and numerical image labels was then used for training and validation of the CNN in an 80%-20% train-test split.

The simulated microstructure, shown in Fig. 7 and labeled by the algorithms interface, exhibits key features of importance to be learned by the classification schema. It was found that the presence of layered dislocations, extensive edge cracking, grain boundary dissociations, and the formation of internal voids in both the crystallite and grain boundary regions of the nanocrystalline material resulted in a highly active and complex microstructural landscape. The diversity and complexity of these microstructural features provide a sufficient classification challenge to provide validation of the algorithmic framework.

In the test case, classified images were presented in palleted scale in order to highlight prominent features. From Fig. 8 it can be seen that images were classified more accurately when more prominent and distinct features were present in the microstructures, in contrast to those which had more a more homogenous distribution of elements. This result is expected and can inform the preparation of samples or simulated microstructures for analysis. Techniques, such as etching, that can be used to highlights features such as grain boundaries or material interfaces are particularly helpful in improving the classification accuracy of the CNN.

While the accuracy of the model is largely dependent on the consistency of the labeling schema used to train the network, relatively high accuracy has been achieved, in terms of precision, F1 score, and recall, on the test dataset.

Validation over the test dataset, corresponding to 20% of the total dataset, resulted in the classification of 10,000 total images with 8,984 of which being correctly classified by the algorithm, resulting in a 89.84% total classification accuracy in the test case as can be seen in the classification report of Fig. 9. This process was repeated five times with randomly assigned train-test splits of the same ratio of 80%-20%, with a variance in accuracy of 1.19% meaning that the algorithm generalized well across the dataset without prevalent overfitting. The accuracy statistics corresponding to each of the classes in the dataset, as well as the total test dataset were presented through the use of a classification report generated by the Sklearn API where precision is inversely related to the false positive rate, recall is directly related to how many of the classes true members are correctly identified, and F1-score which is the weighted average of the two.

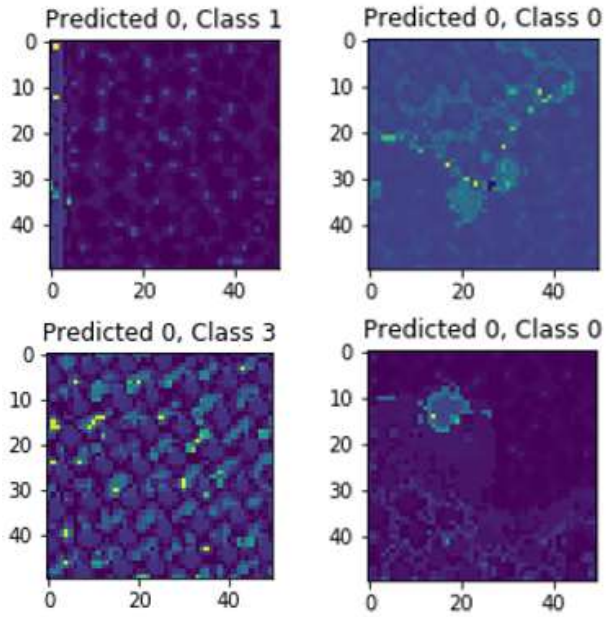

Figure 8. Resultant classified images denoting correctly and incorrectly classified features.

It can be seen from the classification report (Fig. 9) that all classes, with the notable exceptions of 0 and 6, are well above an F1-score of 0.80 meaning that neither false positives or false negatives are of high occurrence in most cases. Class 0, in this case corresponding to a microstructural grain boundary, exhibited a high occurrence of false positives as shown by a low precision meaning that some images were incorrectly classified as class 0, when in fact they weren't. This may be attributed to the high degree of similarity between this class and that of class 6, corresponding to a grain boundary delamination or crack, which exhibited a low recall score meaning that not all true occurrences of this class were correctly labeled as such. The combination of these two phenomena suggests that true members of class 6 were somewhat commonly incorrectly labeled as class 0 due to the similarities in the classes.

```
Found  8984  correct labels
Found  1016  incorrect labels
              precision    recall  f1-score   support

     Class 0       0.69      0.92      0.79      1000
     Class 1       0.99      0.98      0.99      1000
     Class 2       0.89      0.81      0.85      1000
     Class 3       0.90      0.92      0.91      1000
     Class 4       0.85      0.83      0.84      1000
     Class 5       0.99      0.98      0.98      1000
     Class 6       0.82      0.64      0.72      1000
     Class 7       0.96      0.95      0.95      1000
     Class 8       0.99      0.99      0.99      1000
     Class 9       0.96      0.97      0.97      1000

    accuracy                           0.90     10000
   macro avg       0.90      0.90      0.90     10000
weighted avg       0.90      0.90      0.90     10000
```

Figure 9. Sci-kit Learn classification report, denoting the classification performance of the algorithm over each feature set.

Training and validation accuracy, assessed as the ratio of correctly labeled images to total images in each the training (80% split) and testing (20% split) data as plotted in Fig. 10 as a function of epoch can be used to assess the increase in model accuracy during training and the presence of overfitting in the model. In this case a steady increase in

accuracy can be seen for both portions of the dataset meaning that the model is accurately learning the classification relationship. Because the accuracy does not diverge between the two datasets or decrease during training overfitting is not prevalent in the model meaning that the learned classification relationship generalizes well across the datasets.

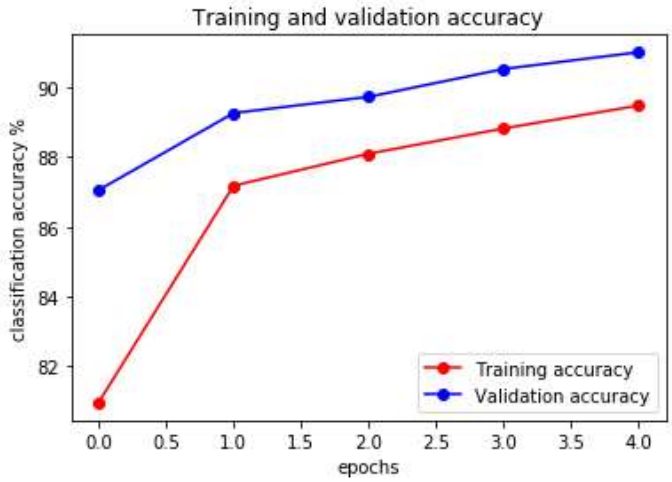

Figure 10. Algorithm classification accuracy evolution by epoch. Matching trend between training accuracy and validation accuracy denotes lack of overfitting.

5. Conclusion

In order to identify features of importance in material microstructural images a Convolutional Neural Network coupled with a set of image processing techniques was implemented in Python. The framework was developed as a black-box model, general and usable across material classes and input data formats. Accuracy and computational efficiency was achieved by utilizing an image-based approach with a dropout operator on numerically encoded tiled image data. Over the test dataset, consisting of nanocrystalline Al-Mg simulated microstructures under tension, the algorithmic framework was successful in accurately identifying prominent microstructural features of interest on a variable length scale at an average classification accuracy of 89.84% at a variance of 1.19%. As such, the framework is of value to research and industry alike in order to facilitate rapid feature analysis of both simulated and test samples and both image and video feed data.

IV. Paper 4

Automated Alloy Design by Coupled Neural Network and Genetic Algorithm

Jacob Hohl[1,*], **Leslie T Mushongera**[1,*]

[1]*Department of Chemical & Materials Engineering, University of Nevada, Reno, Reno, NV, 87557, USA*
**Corresponding authors: lmushongera@unr.edu, johl@unr.edu*

Abstract – Due to the complex nature and expense of traditional high entropy alloy testing and design, a computational system that can facilitate the automated design and optimization of these alloys with consideration to trade-offs in properties and cost is of great value. In order to facilitate this goal, a Regression Neural Network (RNN) is coupled to a Non-dominated Sorting Genetic Algorithm (NSGA-II) in order to propose material designs, assess their efficacy in terms of superior material properties, and optimize their characteristics. The framework is structured to be fully automated and generalizable across datasets and material classes with a single user interface point of the input data file that may be edited to each use case. This algorithmic framework can be used to facilitate the rapid and cost-effective prototyping of new materials of superior performance. The framework was trained and validated over a dataset of 370 High Entropy Alloys consisting of uniaxial tension test data. Designed alloys, generated by the framework, were found to match trends seen in experimental data for both high entropy and low entropy (conventional) alloys.

1. Introduction

High entropy alloys (HEAs), typically comprised of up to twelve alloying components, inherently present a difficult design challenge. Because of the high number of possible alloy compositions, individually creating and testing each material is prohibitively expensive. Even though a good number of HEAs have been developed for various applications, it appears that most of these alloys are suboptimal. Typically, HEA's require costly and time-consuming processing methods to create, and are difficult to accurately characterize. As such, it is hypothesized that a significant number of potentially highly viable materials have not yet been created or tested. This presents an opportunity for significant improvements in the attainable best properties in this class of materials.

The development of the HEAs has so far mainly relied on the experiment driven trial-and-improve approach which is generally expensive and labor intensive. Apparently, the commercially available alloys are the result of many decades of empirical development, and whilst they have good properties, they do not necessarily offer the desired properties, or the right balance of properties needed for specific engineering applications. The conventional trial-and-improve approach centers on selecting the major elements based on the need to satisfy a specific property requirement and further adding alloying components to trigger secondary properties without sacrificing the primary property. This approach however fails to capture the inherent complexity of most real-world problems wherein compromises and trade-offs are required. Considering that up to a dozen elements can enter the composition of HEAs, the complexity of the design problem becomes apparent when considering the huge design space of possible compositions on the one hand and the many conflicting design goals on the other.

Previously, automatic design of complex alloys has been approached by employing physics-based modeling techniques, such as CALPHAD and Molecular Dynamics, alongside traditional machine learning algorithms, such as Support Vector Machines and Random Forests, as well as some deep learning methods [49–52]. However, these methods are limited in their application to high entropy alloys as complex interaction effects, in addition to crystal structure, determine the properties of these materials. These interaction effects are not well known and are therefore typically approximated from known properties of low entropy alloys. As such, CALPHAD and Molecular Dynamics typically lack absolute accuracy while their trends may predict correctly. Attempts to more accurately approximate the interaction effects present in High Entropy Alloys through the use of CALPHAD and MD are limited by the computational cost of such calculations. Support Vector Machines and Random Forests are both more computationally efficient methods of indirectly capturing the dynamics of these materials in order to map material composition to properties but are lacking in resolution and accuracy. They are also not capable of automated generative design, meaning that solutions may be assessed with some accuracy, but not automatically altered to improve performance of the materials. As a significant increase in prediction accuracy and automated optimization capability in recent years, Neural Networks in conjunction with Genetic Algorithms have been proven successful in achieving automated alloy design [53,54]. However, as of yet, an automated design process has not been proposed to accurately optimize across a trade-off in material properties and cost. As such, commercial and academic viability of the proposed alloys is limited.

In this work, we present a system comprised of a coupled Regression Neural Network and Non-dominated Sorting Genetic Algorithm implemented in Python and validated over

a set of high entropy alloy test data that can optimize material properties in relation to their trade-off with alloy cost. The computational framework was established to be adaptable and general across material classes with a static input and output data format. This was done by fully interlinking the two algorithms with a single user interface point being the input data file. By editing this data file the material system and training and validation datasets are defined and the algorithm's parameters are fully specified. By proposing an automated material design system, based on machine learning and driven by material test data, the search space of all possible high entropy alloys can be rapidly explored. Pareto sets of best alloys, as a function of their trade-off in material properties and cost, can be quickly created and then screened by phase field modeling or evaluated by traditional testing procedures allowing for the rapid attainment of reliably and quickly designed superior alloys.

Section 2 will provide some background on the computational framework including Backpropagation Neural Networks and Multi-Objective Genetic Algorithms, the specific implementation and data representation used in this study will be presented in Section 3. Section 4 will introduce the data sets on which the computational framework was validated. The results of this evaluation, as well as an investigation regarding the feasibility of the results will be discussed. Finally, conclusions and next steps are discussed in Section 5.

2. Framework Components and Structure

The structure of the model is based on a coupled Feed-forward Backpropagation Regression Neural Network (Figure 1) and Non-dominated Sorting Genetic Algorithm (Figure 2). The neural network takes the role of a property predictor based on the composition of each proposed material while the genetic algorithm takes the generative role of proposing design solutions and optimizing them based on objective functions of cost and the properties predicted by the neural network. As such, the coupled algorithm is both capable of proposing design solutions and assessing their efficacy.

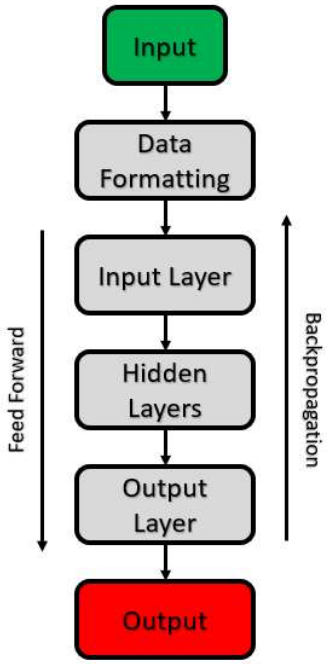

Figure 1. Feedforward Backpropagation Neural Network.

2.1 Neural Network: The Backpropagation Regression Neural Network is employed to map the input data of material composition to the output data of predicted material strength. This algorithm works by stacking input, hidden, and output layers into a fully connected structure to form the pattern recognition process. In this format, the pattern recognition schema is encoded by the weights of individual neurons in the network's layers. During

training of the algorithm, each neuron in the hidden layers has an associated weight that is optimized via gradient descent and backpropagation to iteratively encode the mapping between input (composition) and output (predicted properties).

The input data used by the Neural Network is in the format of composition data by element for each alloy coupled to tested strength, density, and strength density. The data is split into an 80%-20% ratio of training and validation data respectively. The training component of the input data is then multiplied by a set of network weights in the input layer in order to form the first hidden layer. This process is repeated for each subsequent hidden layer sequentially until the output layer is reached. Prior to the output layer, the final hidden layer's output is passed through a nonlinear sigmoidal activation function to form the final prediction. This prediction is then compared with known values of the output parameter and the error between the predicted and true value is backpropagated through the network in order to update individual weights by partial differentiation to iteratively improve the model's prediction performance [55].

2.2 Genetic Algorithm: The Non-dominated Sorting Genetic Algorithm was employed to optimize the characteristics of the designed materials across multiple objectives, in this case a trade-off in strength and cost. To achieve this goal, an original implementation of the NSGA-II algorithm was used [56]. This implementation was chosen due to its relative simplicity and strong optimization performance over multiple objectives. This algorithm works by utilizing evolutionary operators to evolve a population of proposed alloys to optimize their performance as defined by their objective functions, in this case strength density (predicted by the Neural Network) and directly calculated cost density. As such,

the final design set of alloys, being the best members of the final population of the Genetic Algorithm, represents the best trade-off in strength and cost density.

In order for NSGA-II optimization to occur, a clearly defined set of objective functions must be available. In this case, two separately trained instances of the previously defined Neural Network are used to establish the first objective function, either absolute tensile

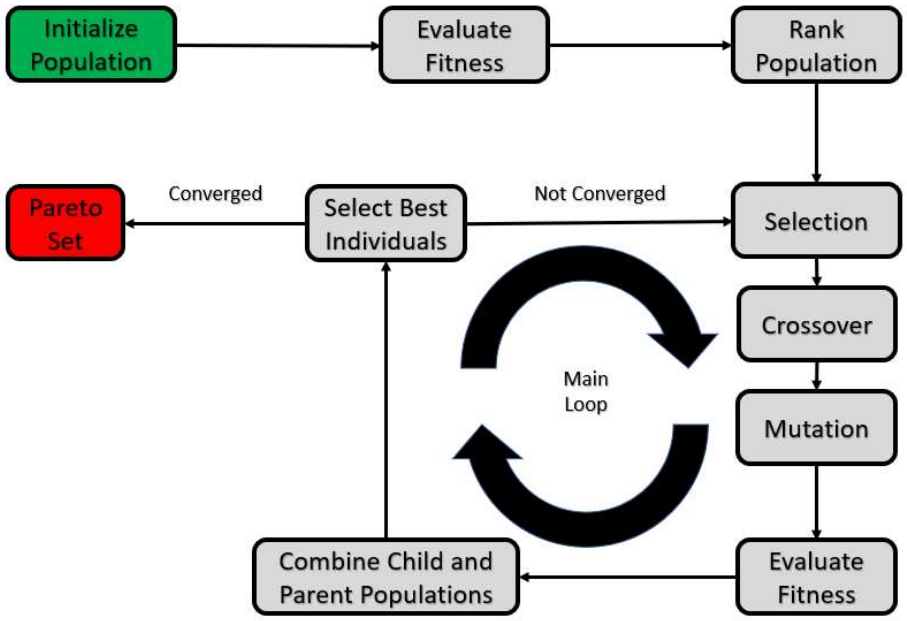

Figure 2. Non-dominated Sorting Genetic Algorithm.

strength or tensile strength density. This objective function works by mapping the composition of each proposed alloy to its predicted strength or strength density. Cost density, as the second optimized objective, is treated as negative cost associated with the amount of each alloying element in a proposed material. In this way, negative cost can be maximized to reduce the necessary expenditure per kilogram of material. In order to compare the efficacy of solutions in a pairwise manner the concept of solution domination is used; an individual of a given population is considered to "dominate" another individual

if its trade-off in properties is superior. That is, in our case, any specific alloy at a higher strength at the same cost as another is considered dominant.

In the event that this sorting criterion alone is insufficient, such as the case where both of the compared individuals are members of the Pareto set, crowding distance sorting is used to retain population diversity during selection and avoid optimizing to a local minima or maxima rather than global optimums. This is done by preferentially selecting individuals from each population that have high crowding distances. This parameter is calculated as a normalized cuboidal distance of each individual from its neighbors in the feature space. By this definition, crowding distance then quantifies how different the given solution is from other solutions in the population. Furthermore, solutions must be feasibly constrained, in this case the constraint that each alloy's total material amount, as set by a sum of each alloying component's composition, is 100% is set by introducing a penalty function in the optimization algorithm. The fitness of each proposed solution is reduced by an amount corresponding to its violation of this constraint function. As such, as the number of generations tends towards the maximum number of generations in the algorithm, the constraint function is increasingly satisfied.

The first generation of the Genetic Algorithm is initialized randomly, in this case each of an individual's eight possible alloying elements' (Al, Co, Cr, Fe, Ni, C, Si, Mo, Nb) compositions are randomly set without constraint, meaning that the total amount of material can exceed 100%. Throughout the subsequent generations of the algorithm, the constraint of 100% total material quantity is set by the aforementioned penalty function. Evaluation of each proposed alloy's fitness is done through the use of each objective function. The chromosomal encoding of alloy composition is used as input for each

objective function, and the corresponding strength, strength density, and cost density is returned from the functions. In this way a fitness value is established in order to guide ranking of the population through the concepts of solution domination and crowding distance.

Selection of parents from the current generation, in order to create the offspring of the next generation, is then carried out through this ranking system. This is done through tournament selection. This process stochastically selects subgroups from the current population and then further sub-selects the best individual of that subgroup as a parent of the next generation. This selection process is repeated for the number of tournaments required to fill a parent population that is twice the size of the current generation. These parents are then recombined through crossover to form the child generation. This is done through single point crossover of two parent's chromosomes. Half of each parent's genes are present in the child alloy, split at the midpoint of the original chromosomes. The population of child alloys is then assigned random mutations in order to preserve population diversity and introduce new possible solutions into the chromosomal encodings. This is done by randomly varying a single gene of a chromosome chosen at random at a set probability. In this case, each gene in the entire population has a set probability of mutation, the mutation amount (amount of change in composition) is also chosen randomly as a value between 0 and 10% composition.

3. Implementation and Dataset

The coupled algorithm was implemented in Python 3.7 with the use of the Sci-kit Learn, Keras, and Pymoo API's. The Neural Network was implemented as a 32 node 4-layer network trained over 100 epochs in batches of 10, with RelU activation functions and a

mean squared loss estimator. The input data for the network was comprised of 8 parameters and one predicted value, and underwent a 80%-20% train-test split. The Non-dominated Sorting Genetic Algorithm was implemented as a 2 objective 2 constraint optimizer over 8 parameters and 1,000 generations of 10,000 individuals.

The material dataset used to train and validate the coupled algorithm is comprised of high entropy alloy composition data describing each material's content of alloying elements coupled to test data describing each material's mechanical properties. These data, described in [57], were collected over a period spanning from 2004 to 2016 from uniaxial tension tests on 370 alloys. This dataset was chosen for validation of the framework due to the fact that it represents one of the most robust freely available datasets for advanced alloys.

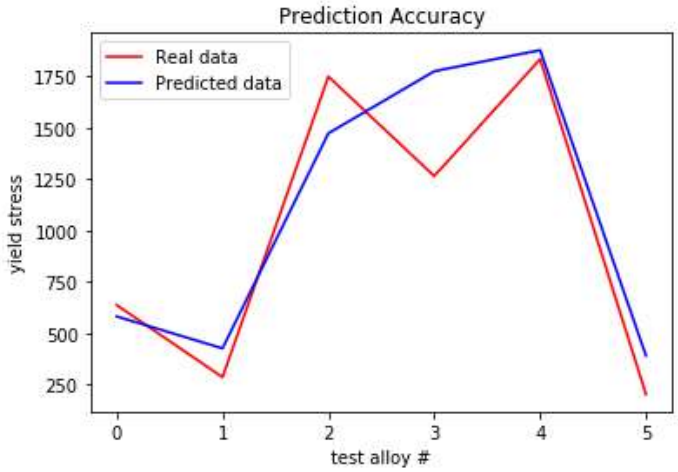

Figure 3. Sample of the prediction results of the Neural Network.

4. Results and Discussion

4.1 High entropy alloys: As the first component of the prediction and optimization framework, the accuracy of the Neural Network's strength predictions must be validated against test data, a subset of the results of this process can be seen in Figure 3.

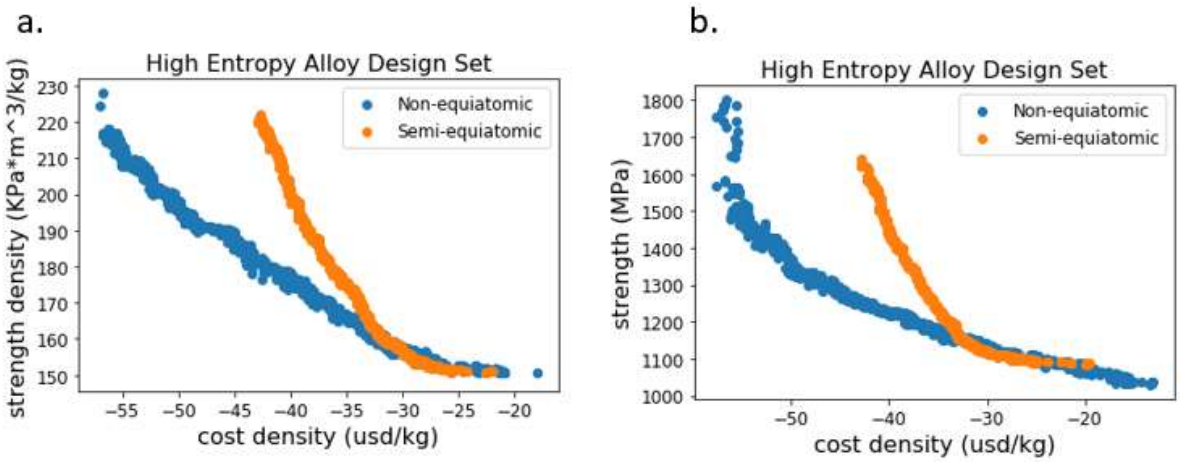

Figure 4. Alloy designer results summary (a) designed high entropy alloy Pareto sets in terms of strength density and (b) in terms of absolute tensile strength.

Five test alloy cases are presented here to illustrate the scatter in accuracy; four of these test cases are shown to track quite well between test and prediction data while one test case shows significant deviation. While this ratio of high prediction performance to deviation tracks throughout the entire 370 alloy dataset, overall prediction accuracy, including these points of deviation, was found to be upwards of 92% over 1000 epochs of the algorithm. By assessing results of the framework in terms of both absolute tensile strength and tensile strength density related to cost density, commercial and economic viability of the proposed alloys can be

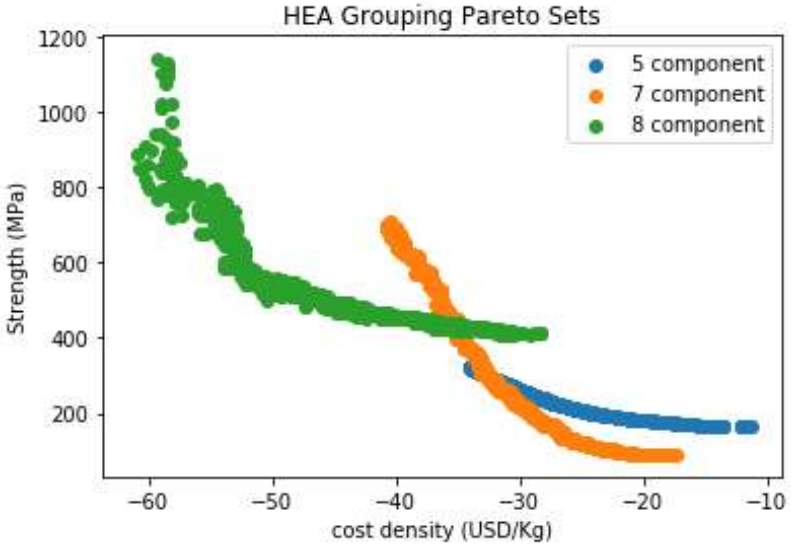

Figure 5. Pareto sets of designed alloys by number of alloying elements, 5, 7, and 8 components.

accurately compared. High entropy design sets were created for both strength and strength density and for five, seven, and eight component alloys.

Trends in the resultant pareto sets, seen in Figure 4, were found to be consistent with expected alloy performance. Semi-equiatomic high entropy alloys, as defined by their major components being within 1% of each other, were found to exhibit higher cost-based performance, while having equal absolute performance, to non-equiatomic high entropy alloys. This is consistent with expected results as non-equiatomic alloys must include a high portion of higher performance costly alloying components to achieve similar strength.

It can be seen from Figure 5. that an increasing number of alloying elements yields stronger performance at the extremes of each Pareto set. This is an expected result as the 7-component set included both Si and Mo, and the 8-component set saw the addition of Nb. These elements are on the high end of the cost spectrum while also providing significant increases to alloy strength in higher contents. As such, the extreme members of each Pareto set include high proportions of these elements, driving up both strength and cost. However, it can also be seen that there is a significant overlap in the 7 component and 8-component Pareto sets. This shows that some members of the 7-component set are strongly Pareto optimal over the worst members of the 8-component set. This means that the designed alloys in this region of the 7-component set are very high strength solutions at low cost.

Al	Co	Cr	Fe	Ni	C	Si	Mo	Nb	Cost Density	Streng
0.00	0.01	0.00	0.43	0.29	0.04	0.01	0.00	0.31	-23.27	1094.8
0.00	0.06	0.00	0.27	0.42	0.09	0.00	0.00	0.25	-23.34	1095.3
0.00	0.19	0.00	0.27	0.40	0.00	0.00	0.00	0.19	-23.85	1098.0
0.00	0.16	0.00	0.23	0.50	0.04	0.01	0.01	0.15	-21.60	1087.4
0.00	0.17	0.00	0.19	0.56	0.00	0.02	0.00	0.13	-21.71	1091.2
0.00	0.17	0.00	0.19	0.56	0.00	0.02	0.00	0.13	-21.71	1090.8
0.01	0.10	0.00	0.00	0.27	0.00	0.00	0.00	0.69	-49.74	1354.2
0.00	0.00	0.00	0.31	0.32	0.00	0.00	0.01	0.42	-30.89	1148.9
0.00	0.17	0.00	0.07	0.52	0.00	0.00	0.01	0.29	-31.14	1149.1
0.00	0.12	0.01	0.08	0.22	0.02	0.02	0.00	0.63	-45.95	1312.3
0.01	0.23	0.00	0.04	0.22	0.01	0.00	0.00	0.59	-46.64	1312.4

Table 1: Portion of Pareto set of designed alloys, unrestricted high entropy alloy dataset.

From Table 1 it can be seen that the unrestricted 8-component design set of alloys retains relatively high levels of diversity, meaning that the optimizer and predictor are robust against overfitting. However, a clear trend in the results can be observed in Figure 6. Of the high entropy alloys present in the resultant Pareto sets, high contents of Iron, nickel, and niobium were found to be present in the majority; in some cases an additional high content of cobalt was present. This combination of elements is expected in optimal alloys and can lead to improved material properties beyond strength. Niobium specifically is commonly added to alloys of iron and nickel base elements in order to promote high temperature stability and resistance to corrosion. Additionally, aerospace superalloys and refractory high entropy alloys have shown that microstructural stability and stability against the precipitation of additional phases is generally high for parings of iron-nickel-niobium.

It can also be seen that an increase in both strength and cost of the designed alloys can be attributed to additional contents of niobium, as seen in the latter half of Table 1. These alloys have approximately double the content of the less strong less costly members of the Pareto set. This trend suggests that an addition of high contents of Niobium to the alloys presents a higher level of absolute performance. Furthermore, it can be seen that contents of silicon, carbon, chromium, and aluminum are low, in some cases below 1%. This is an

expected result as Aluminum does not have the strength necessary to be present in the strongest alloys of the Pareto set. Additionally, Si, C, and Cr, are all alloying elements that are typically added to both high entropy and low entropy alloys in small amounts in order to improve corrosion resistance, strength, and ductility. These results indicate that the optimization performance of the framework is strong, and consistent with previous experimental studies.

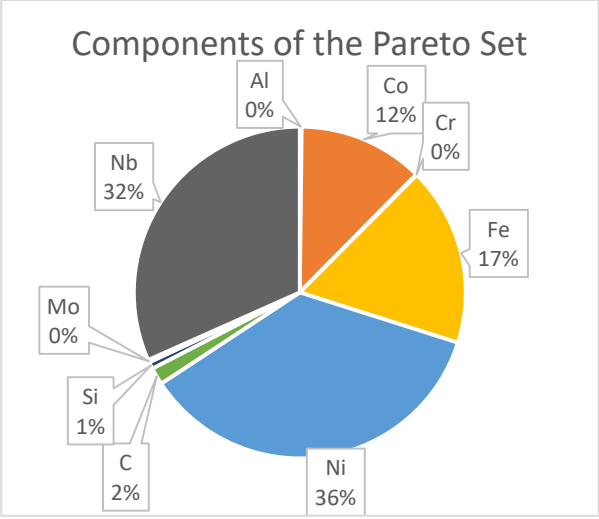

Figure 6. Graphical representation of the Pareto set. Values represent the total amount of each element in all materials in the Pareto set.

4.2 Low entropy alloys: Low entropy alloy sets were designed for each base element in order to facilitate comparisons between the datasets and validation checks of the results across another alloy class. Low entropy alloy results show consistent trends across datasets and metrics. It can be seen from Figure 7 that aluminum and chromium-based alloys both exhibit high absolute strength while aluminum based alloys show a significant advantage in strength density. The relative performance of each base alloy class is consistent with expectation and illustrates the adaptability of the framework to additional datasets. The highest strength density members of this high performing set of aluminum alloys primarily included alloys with above 90% Aluminum content and approximately 1% of each other alloying element. Thermodynamic modeling of these highly multi-component low entropy aluminum alloys is currently an area of ongoing research [58]. While the establishment of a thermodynamic database and comprehensive set of phase diagrams for these alloys

currently limits research progress in the field, they have been shown to be promising candidates for advancements in aerospace engineering and biological implants. To this end, further research into these alloys has been predicted to be promisingly valuable by the

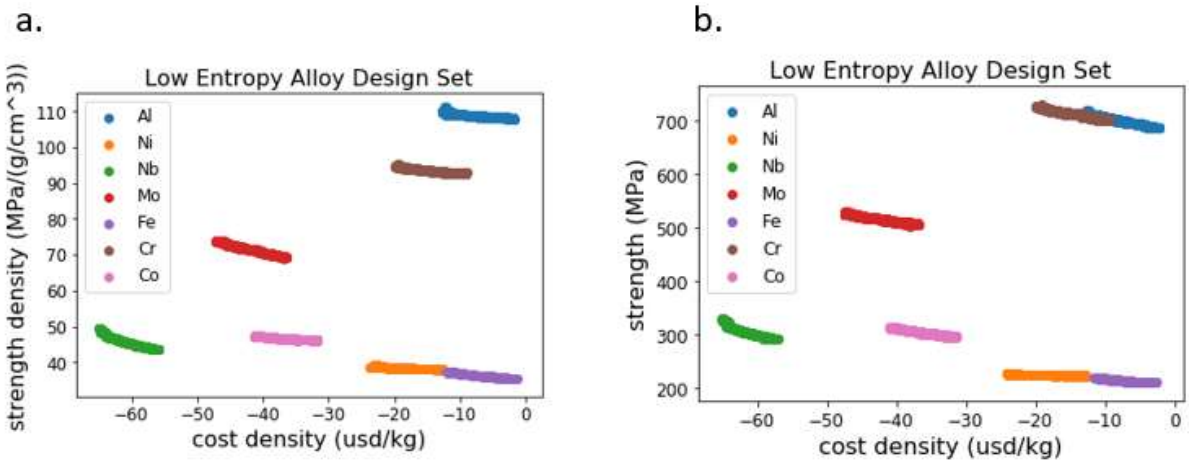

Figure 7. Alloy designer results summary for low entropy alloy case (a) designed low entropy alloy Pareto sets in terms of strength density and (b) in terms of absolute tensile strength.

framework in this work, which is shown to be consistent with the efforts of the authors, and others mentioned, in [58]. Additionally, chromium-based, or high chromium, alloys have been shown by experimental literature to be a relatively strong and low-cost option for highly corrosion resistant materials. Additionally, these alloys have high melting points and relatively low densities for their strength; as such, they have been identified as promising candidates for aerospace engine turbines [59]. In both experimental literature and the design alloy set from this work Cr-Ni-Al alloys are the primary members of the highest performing portion of the Pareto set. From these two classes of low entropy alloys, it can be seen that the framework presented here performs well and is consistent with experimental results not only for the High Entropy Alloy dataset initially used in the study, but across general material datasets. By tailoring the training dataset for the Neural Network portion of the framework to each specific material class, it is expected that high

prediction and optimization performance can be retained for any class of materials that sufficient data is available.

5. Conclusion

Traditional high entropy alloy testing and design poses a significant time and cost challenge. By facilitating the automated design and optimization of these alloys, significant development in the best performance of these material may be enabled. In order to facilitate automated design of high entropy alloy designs according to their trade-offs in material properties and cost a computational framework was proposed based on a coupled Regression Neural Network and Non-dominated Sorting Genetic Algorithm. Strong prediction and optimization performance was found over a dataset of 370 high entropy alloys. Additionally, the framework was proven to be adaptable to additional datasets and classes of materials. Therefore, the work herein presents a framework and methodology for efficient design of viable high entropy alloys and other material classes.

8. Thesis Conclusion and Recommendations

The design and optimization of metallic alloys poses a significant challenge due to the complexity of interaction effects between components and the size of the search space of all possible alloys. To address this challenge, three computational frameworks alongside a Molecular Dynamics study were proposed. An ab initio nanocrystalline alloy thermodynamics framework was developed to assess the stability of binary nanocrystalline Al-X alloys against grain enlargement and phase precipitation, Molecular Dynamics studies were conducted in order to quantify the deformation mechanisms in these materials,

a Convolutional Neural Network was utilized to analyze microstructural image data, and a coupled Neural Network and Multi-objective Genetic Algorithm was applied to automatically generate, assess, and optimize alloy designs. By developing these systems and validating them over a dataset of binary nanocrystalline Aluminum alloys and multi-component High Entropy Alloys significant portions of the alloy design, optimization, and analysis process have been automated. For this reason, this research may be used by academia and industry alike to decrease development times and increase research productivity.

In order to extend this work and further broaden the scope of application and capability of this branch of research, and the frameworks developed herein, it is recommended that they be applied to additional material systems. By conducting these studies, a scope of applicability may be identified, and the algorithms may be improved to encompass additional pre and post-processing mechanisms for different datasets. Additionally, important mechanisms of specific material systems may be elucidated by the results produced from that process. Furthermore, conducting further Molecular Dynamics studies for additional loading cases of nanocrystalline microstructures and post-processing the resulting simulated structures through the use of the CNN-based framework would provide valuable insight into the mechanics of this class of materials. This work is an important step towards the commercialization of nanocrystalline metals.

9. References

[1] Y. Gutkin, Nanostructured Metals and Alloys Processing, Mechanical Properties and Applications, Met. Surf. Eng. Woodhead Publishing Series (2011) 329–374.

[2] I. Ovid'ko, Review on superior strength and enhanced ductility of metallic nanomaterials, Prog Mater Sci. (2018) 462–540.

[3] B. Han, Improvement of toughness and ductility of cryomilled Al-Mg alloy via microstructural modification, Met. Mat Trans A. (2005) 2081–2091.

[4] V.L. Tellkamp, E.J. Lavernia, Processing and mechanical properties of nanocrystalline 5083 Al alloy, Nanostructured Mater. 12 (1999) 249–252.

[5] K.M. Youssef, R.O. Scattergood, K.L. Murty, C.C. Koch, Nanocrystalline Al-Mg alloy with ultrahigh strength and good ductility, Scr. Mater. 54 (n.d.) 251–256.

[6] S. Pun, Nanocrystalline Al-Mg with extreme strength due to grain boundary doping, Mater. Sci. Eng. (2017) 400–406.

[7] L. Mishnaevsky, E. Levashov, Micromechanical modelling of nanocrystalline and ultrafine grained metals: A short overview, Comput. Mater. Sci. (2015) 365–373.

[8] H. Gleiter, Nanostructured materials: basic concepts and microstructure, Acta Mater. 48 (2000) 1–29.

[9] Garritt J. Tucker, David L. McDowell, Non-equilibrium grain boundary structure and inelastic deformation using atomistic simulations, Int. J. Plast. 27 (2011) 841–857.

[10] S. Divinski, H. Rosner, G. Wilde, Functional Nanostructured Materials - Microstructure, Thermodynamic Stability and Atomic Mobility, Front. Nanosci. 1 (2009) 1–50.

[11] J. Tamaki, K. Fujimori, M. Akiyama, N. Harada, N. Miura, N. Yamazoe, Grain-size effects in tungsten oxide-based sensor for nitrogen oxides, J. Electrochem. Soc. (1994).

[12] J. Westbrook, D. Wood, Embrittlement of grain boundaries by equilibrium segregation, Nature. (1961).

[13] J. Luo, V. Gupta, D. Yoon, H. Meyer, Segregation-induced grain boundary pre-melting in nickel-doped tungsten, Appl. Phys. (2005).

[14] A. Devaraj, W. Wang, R. Vemuri, L. Kovarik, X. Jiang, M. Bowden, J.R. Trelewicz, S. Mathaudhu, A. Rohatgi, Grain boundary segregation and intermetallic precipitation in coarsening resistant nanocrystalline aluminum alloys, Acta Mater. 165 (2019) 698–708.

[15] She Peng, Yujie Wei, Huaijian Gao, Nanoscale precipitates as sustainable dislocation sources for enhanced ductility and high strength, PNAS. 117 (2020) 5204–5209.

[16] A. Joshi, C.R. Shastry, M. Levy, Effect of Heat Treatment on Solute Concentration at Grain Boundaries in 7075 Aluminum Alloy, Metall. Trans. A (1981) 1081–1088.

[17] R.K. Viswanadham, T.S. Sun, J.A.S. Green, Grain boundary segregation in Al-Zn-Mg alloys - Implications to stress corrosion cracking, Metall. Mater. Trans. A (1980) 85–89.

[18] A.K. Vasudevan, R.D. Doherty, Grain boundary ductile fracture in precipitation hardened aluminum alloys, Acta Metall. 35 (1987) 1193–1219.

[19] Michael J. Moran, Howard N. Shapiro, Daisie D. Boettner, Margaret B. Bailey, Fundamentals of Engineering Thermodynamics, 8th ed., Wiley, n.d.

[20] Mingming Gong, Fnag Liu, Yuzeng Chen, Thermal stability of nanocrystalline materials: thermodynamics and kinetics, Int. Mater. Rev. (n.d.).

[21] J. Weissmuller, Alloy effects in nanostructures, Nanostructured Mater. (1993) 261–272.

[22] R. Birringer, Metastable Phase Formation in the Solid State, Klost. Irsee. (1992).

[23] F. Liu, R. Kirchheim, Nanoscale grain gowth inhibited by reducing grain boundary energy through solute segregation, J. Cryst. Growth. (2004) 385–391.

[24] J. Trelewicz, C. Schuh, Grain Boundary Segregation and Thermodynamically Stable Binary Nanocrystalline Alloys, MIT Phys. Rev. B. (2009).

[25] M. Saber, H. Kotan, C.C. Koch, Thermodynamic stabilization of nanocrystalline binary alloys, J. Appl. Phys. (2013).

[26] T. Chookajorn, H. Murdoch, C. Schuh, Design of Stable Nanocrystalline Alloys, Science. (2012).

[27] H. Murdoch, C. Schuh, Stability of Binary Nanocrystalline Alloys Against Grain Growth and Phase Separation, Acta Mater. (2013).

[28] M. Saber, H. Kotan, C.C. Koch, A predictive model for thermodynamic stability of grain size in nanocrystalline ternary alloys, J. Appl. Phys. (2013).

[29] H. Murdoch, C. Schuh, Estimation of Grain Boundary Segregation Enthalpy and its role in stable nanocrystalline alloy design, J. Mater. Res. (2013).

[30] A.R. Miedema, R. Boom, F.R. De Boer, On the Heat of Formation of Solid Alloys, J. Common Met. 41 (1975) 283–298.

[31] D. McLean, Grain boundaries in metals, Oxf. Clarendon Press. (n.d.).

[32] J. Trelewicz, C. Schuh, The Hall-Petch Breakdown in Nanocrystalline Metals: A crossover to glass-like deformation, Acta Mater. (2007).

[33] H. Murdoch, Design of a Stable Nanocrystalline Alloy, MIT Thesis. (2013).

[34] H. Van Swygenhoven, J.R. Weertman, Deformation in nanocrystalline metals, Mater. Today. 9 (2006) 24–31. https://doi.org/10.1016/S1369-7021(06)71494-8.

[35] V. Yamakov, D. Wolf, S.R. Phillpot, A.K. Mukherjee, H. Gleiter, Deformation-mechanism map for nanocrystalline metals by molecular-dynamics simulation, Nat. Mater. 3 (2004) 43–47. https://doi.org/10.1038/nmat1035.

[36] A. Kobler, C. Brandl, H. Hahn, C. Kübel, In situ observation of deformation processes in nanocrystalline face-centered cubic metals, Beilstein J. Nanotechnol. 7 (2016) 572–580. https://doi.org/10.3762/bjnano.7.50.

[37] J. Hohl, P. Kumar, M. Misra, P. Menezes, L.T. Mushongera, Thermodynamic stabilization of nanocrystalline aluminum, J. Mater. Sci. 56 (2021) 14611–14623. https://doi.org/10.1007/s10853-021-06224-2.

[38] I.A. Ovid'ko, Plastic deformation mechanisms in nanocrystalline metallic materials:, J. Mech. Behav. Mater. 22 (2013) 81–88. https://doi.org/10.1515/jmbm-2012-0005.

[39] A. Campbell, P. Murray, E. Yakushina, S. Marshall, W. Ion, New methods for automatic quantification of microstructural features using digital image processing, Mater. Des. 141 (2018) 395–406. https://doi.org/10.1016/j.matdes.2017.12.049.

[40] B.L. DeCost, E.A. Holm, A computer vision approach for automated analysis and classification of microstructural image data, Comput. Mater. Sci. 110 (2015) 126–133. https://doi.org/10.1016/j.commatsci.2015.08.011.

[41] S.M. Azimi, D. Britz, M. Engstler, M. Fritz, F. Mücklich, Advanced Steel Microstructural Classification by Deep Learning Methods, Sci. Rep. 8 (2018) 2128. https://doi.org/10.1038/s41598-018-20037-5.

[42] J. Ling, M. Hutchinson, E. Antono, B. DeCost, E.A. Holm, B. Meredig, Building data-driven models with microstructural images: Generalization and interpretability, Mater. Discov. 10 (2017) 19–28. https://doi.org/10.1016/j.md.2018.03.002.

[43] W. Ye, P. Kumar, M. Misra, L.T. Mushongera, Local damage in grain boundary stabilized nanocrystalline aluminum, Mater. Lett. 300 (2021) 130153. https://doi.org/10.1016/j.matlet.2021.130153.

[44] Alex Krizhevsky, Ilya Sutskever, Geoffrey E Hinton, Imagenet classification with deep convolutional neural networks, Adv. Neural Inf. Process. Syst. 25 (n.d.) 1097–1105.

[45] Yann LeCun, Yoshua Bengio, Convolutional networks for images, speech, and time series, Handb. Brain Theory Neural Netw. 3361 (1995) 1–14.

[46] K. O'Shea, R. Nash, An Introduction to Convolutional Neural Networks, ArXiv E-Prints. (2015).

[47] S. Albawi, T. Abed Mohammed, S. ALZAWI, Understanding of a Convolutional Neural Network, (2017). https://doi.org/10.1109/ICEngTechnol.2017.8308186.

[48] B. Xu, N. Wang, T. Chen, M. Li, Empirical Evaluation of Rectified Activations in Convolutional Network, (2015).

[49] U. Masood Chaudry, K. Hamad, T. Abuhmed, Machine learning-aided design of aluminum alloys with high performance, Mater. Today Commun. 26 (2021) 101897. https://doi.org/10.1016/j.mtcomm.2020.101897.

[50] L. Ward, S.C. O'Keeffe, J. Stevick, G.R. Jelbert, M. Aykol, C. Wolverton, A machine learning approach for engineering bulk metallic glass alloys, Acta Mater. 159 (2018) 102–111. https://doi.org/10.1016/j.actamat.2018.08.002.

[51] C. Wen, Y. Zhang, C. Wang, D. Xue, Y. Bai, S. Antonov, L. Dai, T. Lookman, Y. Su, Machine learning assisted design of high entropy alloys with desired property, Acta Mater. 170 (2019) 109–117. https://doi.org/10.1016/j.actamat.2019.03.010.

[52] R. Liu, A. Kumar, Z. Chen, A. Agrawal, V. Sundararaghavan, A. Choudhary, A predictive machine learning approach for microstructure optimization and materials design, Sci. Rep. 5 (2015) 11551. https://doi.org/10.1038/srep11551.

[53] B. Debnath, A. Vinoth, M. Mukherjee, S. Datta, Designing Fe-based high entropy alloy–a machine learning approach, IOP Conf. Ser. Mater. Sci. Eng. 912 (2020) 052021. https://doi.org/10.1088/1757-899x/912/5/052021.

[54] J.-W. Lee, C. Park, B. Do Lee, J. Park, N.H. Goo, K.-S. Sohn, A machine-learning-based alloy design platform that enables both forward and inverse predictions for thermo-mechanically controlled processed (TMCP) steel alloys, Sci. Rep. 11 (2021) 11012. https://doi.org/10.1038/s41598-021-90237-z.

[55] R. Hecht-Nielsen, Theory of the backpropagation neural network, Int. 1989 Jt. Conf. Neural Netw. (1989) 593–605 vol.1.

[56] K. Deb, A. Pratap, S. Agarwal, T. Meyarivan, A fast and elitist multi-objective genetic algorithm: NSGAII, IEEE Trans. Evol. Comput. 6 (2002).

[57] S. Gorsse, M.H. Nguyen, O.N. Senkov, D.B. Miracle, Database on the mechanical properties of high entropy alloys and complex concentrated alloys, Data Brief. 21 (2018) 2664–2678. https://doi.org/10.1016/j.dib.2018.11.111.

[58] Y. Du, S. Liu, L. Zhang, H. Xu, D. Zhao, A. Wang, L. Zhou, An overview on phase equilibria and thermodynamic modeling in multicomponent Al alloys:

Focusing on the Al–Cu–Fe–Mg–Mn–Ni–Si–Zn system, Calphad. 35 (2011) 427–445. https://doi.org/10.1016/j.calphad.2011.06.007.

[59] D. Locq, P. Caron, C. Ramusat, R. Mévrel, Chromium-Based Alloys Strengthened by Ordered Phase Precipitation for Gas Turbine Applications, Adv. Mater. Res. 278 (2011) 569–574. https://doi.org/10.4028/www.scientific.net/AMR.278.569.